Regional Variations of Mercury's Crustal Density and Porosity from MESSENGER Gravity Data

Antonio Genova[1], Sander Goossens[2], Edoardo Del Vecchio[1], Flavio Petricca[1], Mikael Beuthe[3], Mark Wieczorek[4], Gianluca Chiarolanza[5,6], Gaetano di Achille[7], Giuseppe Mitri[5,6], Ivan di Stefano[1], Bernard Charlier[8], Erwan Mazarico[2], Peter James[9]

[1] Department of Mechanical and Aerospace Engineering, Sapienza University of Rome, Rome, 00184, Italy
[2] NASA Goddard Space Flight Center, Greenbelt, MD, USA.
[3] Royal Observatory of Belgium, Brussels, Belgium
[4] Université Côte d'Azur, Observatoire de la Côte d'Azur, CNRS, Laboratoire Lagrange, France
[5] Università d'Annunzio, Pescara, Italy
[6] International Research School of Planetary Sciences, Pescara, Italy
[7] INAF – Osservatorio Astronomico d'Abruzzo, Teramo, Italy
[8] Department of Geology, University of Liège, Sart Tilman, Belgium
[9] Department of Geosciences, Baylor University, Waco, TX 76798

Abstract

A new solution of Mercury's gravity field to degree and order 160, named *HgM009*, is retrieved through a reprocessing of MESSENGER radio science measurements. By combining our latest gravity field with topography data, localized spectral admittance analyses are carried out to investigate Mercury's crustal and lithospheric properties across the northern hemisphere. The measured spectra are compared with admittances predicted by lithospheric flexure models that account for surface loading only. The localized gravity/topography admittance analyses yield key information on the lateral variations of the bulk density of the upper crust. Elastic and crustal thicknesses are also adjusted in our study, but the local admittance spectra allow us to constrain these parameters only over a few regions. The average bulk density across the observed areas in the northern hemisphere is 2540 ± 60 kg m^{-3}. The crustal porosity is then constrained by using an estimate of the pore-free grain density of surface materials with our measured bulk density. Our estimate of the mean porosity is 14.7 ± 1.6 %, which is comparable to, but slightly higher than,

the average value measured on the Moon. Larger crustal porosities are observed over heavily cratered regions, suggesting that impact bombardment is the main cause of the crustal porosity.

1. Introduction

A precise characterization of Mercury's crust is fundamental to determine the events that led to the formation and evolution of the planet. The silicate shell of Mercury preserves a record of the planet's evolution from a primordial fully molten state, to initial crust formation, subsequent impact events and later volcanic processes (Charlier and Namur 2019). The crystallization of the silicate magma ocean might have formed a graphitic floatation primary crust (Vander Kaaden and McCubbin 2015). Later additions to the crust were produced by magmas derived from partial melting of the mantle (Charlier, Grove, and Zuber 2013; Namur et al. 2016). Crater chronology studies suggest that the planet was globally resurfaced by enhanced impact bombardment rates and volcanism ~4 Gyr ago (Fassett et al. 2011; Marchi et al. 2013). Volcanism probably ceased ~3.5 Gy ago (Byrne et al. 2016), leaving a multi-layer structure of the crust that was acquired during about 0.7 Gyr of geologic evolution. These geologic processes can be investigated through an in-depth examination of crustal properties, including density and thickness, from analyses of highly accurate gravity and topography measurements (Wieczorek et al. 2013).

The MErcury Surface, Space ENvironment, GEochemistry, and Ranging (MESSENGER) spacecraft orbited Mercury for more than four years yielding among others, high-resolution gravity and topography maps of the northern hemisphere (Solomon, Nittler, and Anderson 2018). The measured gravity anomalies are induced by different factors including surface relief and sub-surface relief along the crust-mantle and core-mantle interfaces. Surface relief and magmatic intrusions, furthermore, exert a load on the outer layers leading to the flexure of the lithosphere

(*e.g.*, James et al. 2015). The contribution of these effects to the gravity field, however, becomes less important as the spatial wavelength decreases, enabling the recovery of the bulk crustal density through the analysis of gravity/topography correlation and admittance spectra (*e.g.*, Wieczorek et al. 2013).

The Mercury Laser Altimeter (MLA) onboard the MESSENGER spacecraft acquired precise measurements of the surface relief (Zuber et al. 2012). Mercury's gravity field was measured by the MESSENGER radio science team providing updated versions of the estimated field during the mission (Smith et al. 2012; Mazarico et al. 2014). By analyzing the entire mission dataset, the latest global solution, *HgM008*, was retrieved in spherical harmonics to degree and order 100 (Genova et al. 2019), which resolves wavelengths of about 150 km. Independent gravity fields were also presented by other groups to confirm the main geophysical results (Genova, Iess, and Marabucci 2013; Verma and Margot 2016), including the latest solutions that were developed to even higher degrees (Konopliv, Park, and Ermakov 2020).

To extend the resolution of our latest gravity model *HgM008*, two independent techniques have been adopted for the processing of MESSENGER radio science data. A first approach is based on the analysis of the line-of-sight (LoS) accelerations (Goossens et al. 2022) based on the Doppler residuals computed for the *HgM008* solution (Genova et al. 2019). In this study, we present a new gravity field, named ***HgM009***, that was retrieved through the precise orbit determination (POD) of the MESSENGER by reanalyzing the entire radio tracking dataset (*i.e.*, Doppler and range measurements) through refined models of the orbital dynamics. This new global solution is thus used in this work to investigate regional variations of Mercury's crustal density and porosity, and the thickness of the crust and lithosphere.

The data and methods are presented in Section 2 with a description of the gravity measurements that are used in the gravity/topography admittance and correlation analysis. Localized spectral admittances are investigated in Section 3 to determine the crustal density and thickness, and the elastic thickness. A comparison of the bulk density with the surface grain density is discussed in Section 4 to determine a regional map of the surface porosity. Our findings are summarized in Section 5.

2. Data and Methods

2.1Gravity and Topography Modeling

The spatial correlation of both gravity and topography fields with surface geological features (*e.g.*, volcano-tectonic structures, impact craters, and basins) provides key information on the history of the crust. A detailed mapping of surface relief is fundamental for retrieving the topographic load exerted on the outer layers, and gravity anomalies constrain the internal mass distribution beneath the surface. Estimates of crustal thickness and density can be obtained by combining these two geophysical datasets. Consistent representations of both gravity and topography, combined with the surface analysis for their possible association with geological structures, are then required to enhance our knowledge of the planetary crust. Spherical harmonic expansions are adopted for Mercury's gravitational potential, $U(r,\lambda,\theta)$, and topographic relief, $h(\lambda,\theta)$, as follows:

$$U(r,\lambda,\theta) = -\frac{GM}{R}\left\{1+\sum_{l=2}^{l_{max}}\left(\frac{R}{r}\right)^{l}\sum_{m=0}^{l}(\overline{\mathrm{C}}_{lm}cos\ m\lambda\ +\overline{\mathrm{S}}_{lm}sin\ m\lambda\ )\overline{\mathrm{P}}_{lm}(cos\theta)\right\}$$
$$h(\lambda,\theta) = \sum_{l=0}^{l_{max}}\sum_{m=0}^{l}(\overline{\mathrm{C}}^{t}_{lm}cos\ m\lambda\ +\overline{\mathrm{S}}^{t}_{lm}sin\ m\lambda\ )\overline{\mathrm{P}}_{lm}(cos\theta) \quad (1)$$

where GM = 22,031.8635 × 10^9 m^3 s^{-2} is Mercury's gravitational constant estimated in our global solution; and R = 2,440,000 m is the reference radius of the planet; and r, λ, and θ are radial, longitude, and colatitude coordinates, respectively. The pair of parameters $(\bar{C}_{lm}, \bar{S}_{lm})$, and $(\bar{C}^t_{lm}, \bar{S}^t_{lm})$ are fully normalized spherical harmonic coefficients of degree l and order m of the potential and topography, respectively, and $\bar{P}_{lm}$ is the associated normalized Legendre function. The normalization used in geodesy leads to an integral of the squared spherical harmonic functions that is equal to 4π (Wieczorek 2015). The topography used in this study is the model GTMES_150V05 (archived on the NASA Planetary Data System, PDS, at https://pds-geosciences.wustl.edu/messenger/mess-h-rss_mla-5-sdp-v1/messrs_1001/data/shadr/gtmes_150v05_sha.tab) with a mean planetary radius of 2,439,400 m. We note that the spherical coordinate systems of the gravity and topography models are referenced to different planetary orientation models. The latest gravity solutions include adjustments of the pole right ascension and declination, spin rate, and the amplitude of physical librations in longitude, leading to a redefinition of Mercury's rotational state (*e.g.*, Genova et al. 2019; Konopliv, Park, and Ermakov 2020). Mercury's topography is based on the orientation model that was retrieved through the processing of Earth-based radar observations (Margot et al. 2012). Our new estimation of Mercury's gravity field includes the adjustments of the pole's orientation, spin rate and amplitude of physical librations that are fully consistent with our previous *HgM008* field (Genova et al. 2019). The topography was then reoriented to the reference frame defined by our gravity solution to determine localized correlation and admittance spectra. By reorienting the topographic model and gravitational field to a common reference frame, however, we determined that this correction has a negligible effect on our inversions for the crustal density.

2.2 Gravity Field *HgM009*

119 Geodetic investigations from space lead in general to non-uniform spatial resolutions of both
120 gravity and topography data, due to changing orbital characteristics. Altimetry, however, enables
121 a more uniform mapping of the observed regions or areas with multiple measurements that increase
122 the resolution of digital elevation models. Radio science measurements are strongly affected by
123 the spacecraft orbit configuration since the gravity signals weaken with increasing altitudes. The
124 MESSENGER spacecraft orbited Mercury from a highly eccentric orbit covering the planet's
125 latitudes from different altitudes. The orbit periapsis had an initial latitude of ~60ºN enabling low
126 spacecraft altitudes at mid-latitudes in the northern hemisphere (Solomon et al. 2001). Topography
127 data acquired by the MESSENGER mission are limited to the northern hemisphere only, but a
128 global digital elevation model of Mercury has been created from a least-squares bundle adjustment
129 of common features measured in overlapping MESSENGER Mercury Dual Imaging System
130 (MDIS) Narrow Angle Camera (NAC) and Wide Angle Camera (WAC) filter images (Becker et
131 al. 2016).
132 The low-altitude campaign of the MESSENGER mission led to a great enhancement of the gravity
133 field resolution over local mid- and high-latitude regions. During the final year of operations, the
134 spacecraft reached altitudes lower than 50 km above Mercury's surface during radio tracking
135 passages. To analyze the entire MESSENGER dataset including the low-altitude measurements,
136 the gravity field of Mercury was first estimated to degree and order 100 yielding the *HgM008*
137 model (Genova et al. 2019). An independent re-analysis of the MESSENGER data led to the
138 estimation of Mercury's gravity field to degree and order 160, *Mess160a* (Konopliv, Park, and
139 Ermakov 2020). In order to predict the local resolution of the gravity field, we use the degree
140 strength technique (for details see Konopliv, Banerdt, and Sjogren 1999) that compares the
141 expected acceleration profiles with the uncertainties based on the gravity covariance matrix. By

142 expanding our gravity solution to degree and order 160, the degree strength technique shows
143 maximum local resolutions l_{max} equal to 160 (Figure S1), which corresponds to a ~50-km (half-
144 wavelength) spatial resolution over the regions covered by the low-altitude campaign.
145 To enhance our estimate of the short-wavelength anomalies of Mercury's gravity, a new solution
146 was recovered through the processing of the LoS accelerations (Goossens et al. 2022). This data
147 type is based on a numerical differentiation carried out from the standard Doppler residuals, which
148 are the differences between the measurements and the computed observations based on our data
149 and dynamical modeling. The gravity solution presented by Goossens et al. 2022 was obtained by
150 analyzing the LoS accelerations computed from the Doppler residuals resulting from the inversion
151 of the *HgM008* gravity model (Genova et al. 2019).
152 In this study, we reprocessed the entire MESSENGER dataset, which includes Doppler and range
153 measurements, by using a refined modeling of the non-conservative forces in the POD software
154 GEODYN II (Pavlis and Nicholas 2017). Compared to our previous gravity and spacecraft orbit
155 solutions (Genova et al. 2018; 2019), an accurate model of the spacecraft thermal reradiation
156 accelerations is included in the trajectory integration. This refinement of the spacecraft dynamical
157 equations provides significant benefits to the orbit determination results during the low-altitude
158 campaign. The Doppler residuals show an improvement of 5-10% on average compared to our
159 previous POD solution (Genova et al., 2019). A detailed description of the spacecraft thermal
160 reradiation modeling and the POD enhancements are discussed in a separate manuscript in
161 preparation.
162 A key factor in the gravity inversion is the *a priori* constraint applied to the spherical harmonic
163 coefficients for degrees greater than 10. The radio tracking data of the MESSENGER mission are
164 processed through a batch least-squares method, forming normal equations that require the use of

a priori information to enable a smooth inversion of the problem (Tapley, Schutz, and Born 2004). This additional matrix in the normal equations is required because of the uneven coverage of Mercury's surface with MESSENGER radio science data. A common approach to constrain the gravity inversion is based on the use of an empirical Kaula rule that predicts the square root of the degree variance for the high-degree spherical harmonic coefficients (Kaula 1966), as follows,

$$C_l = \sqrt{\frac{1}{2l+1}\left(\bar{C}_{lm}^2 + \bar{S}_{lm}^2\right)} \approx \frac{A_k \times 10^{-5}}{l^2}. \quad (2)$$

This rule was obtained empirically for the power spectrum of Earth's gravity field, by implicitly assuming that the square root of the degree variance of the gravity field is inversely proportional to the maximum elastic stress (Ermakov, Park, and Bills 2018). The numerical constant parameter A_k is scaled for each celestial body by using, for example, the surface gravity. The gravity spectrum associated with the topography-induced field predicts $A_k \sim 4-6$ for Mercury, if the mean crustal density is in the range ρ_c = 2600-2900 kg m^{-3}. A Kaula constraint with A_k equal to 4 and 5 was previously used to determine the gravity fields *HgM008* (Genova et al. 2019) and *Mess160a* (Konopliv, Park, and Ermakov 2020), respectively. The larger the parameter A_k is, the weaker is the constraint used in the gravity inversion. To better investigate the impact of this assumption on the quality of our gravity solutions, we inverted the normal equations while varying the A_k scale factor from 5 to 100 (Fig. 1-a).

Different approaches have also been proposed in the literature to better regularize the gravity solutions. We also applied the degree strength technique to constrain the measured acceleration profiles, which accounts for the local variations in the spatial resolution (Konopliv, Banerdt, and Sjogren 1999). By globally comparing the local strength of the measured gravity field with the assumed Kaula rule (A_k=5), we define a spatially varying *a priori* constraint matrix (Figure S2). An alternative gravity constraint is based on the predicted gravity field induced by topographic

187 relief (Goossens et al. 2017; Konopliv, Park, and Ermakov 2020). By assuming a crustal density
188 ρ_c = 2800 kg m^{-3}, we determined the gravity anomalies induced from topography by using finite-
189 amplitude corrections (Wieczorek and Phillips 1998), and it is then converted in spherical
190 harmonics to be applied as *a priori* formal uncertainty for the gravity inversion. This constraint
191 yields free-air gravity anomalies that correlate better with topography over regions poorly covered
192 by MESSENGER radio science data (Figure S3).
193 To investigate the properties of Mercury's crust and lithosphere, a gravity/topography correlation
194 and admittance analysis is carried out over local regions in the northern hemisphere. Our results
195 suggest that the gravity solution based on the Kaula rule with A_k = 10 (whose free-air anomalies
196 are show in Figure S4) provides higher correlations, which are described in Sec. 2.3, with respect
197 to solutions based on other Kaula rules (Figures S5) or degree strength constraint (Figure S6) or
198 to *HgM008* solution (Figures S7, S8 and S9). Comparable gravity/topography correlations and
199 more stable admittance spectra are obtained with respect to our solution based on the gravity from
200 topography constraint (Figure S6) and to the independent solution *Mess160a* (Figures S7, S8 and
201 S9). The gravity field based on the Kaula rule constraint with A_k = 10, named *HgM009*, is used in
202 our analysis to invert Mercury's crust density and thickness, and the thickness of its lithosphere.

203 ## 2.3 Correlation and Admittance Analysis

204 The bulk density of the upper crust is one of the parameters that can be determined from
205 analyses of gravity/topography correlation and admittance spectra. Short-wavelength topographic
206 signals induce very little lithospheric flexure, and a precise determination of high-degree spherical
207 harmonic coefficients of both gravity and topography allows one to constrain the bulk density of
208 the upper portion of the crust.

209 Topographic loading induces lithospheric flexure that deflects the crust-mantle interface, with the
210 relative amount of flexure decreasing with increasing spherical harmonic degree. The lithosphere
211 only flexes slightly at the shortest wavelengths, and the gravity-topography admittance is not
212 sensitive to the elastic thickness (T_e) at sufficiently high degrees (Wieczorek et al. 2013). This
213 asymptotic behavior depends on the celestial body; for example, the contribution of the elastic
214 thickness to the admittance is negligible above degree 150 for the Moon (Wieczorek et al. 2013)
215 but lithospheric flexure can contribute to the admittance spectrum up to degree 300 for Mars
216 (Goossens et al. 2017). Figure 2 shows theoretical admittance between gravity and topography
217 (Turcotte et al. 1981; see below for details about this admittance model) for models with varying
218 elastic thickness or crustal density only, with a fixed crustal thickness. We find that different
219 lithospheric thicknesses do not significantly affect the admittance spectrum beyond degree 200.
220 The resolution of Mercury's gravity field over the northern hemisphere indicates that it is sensitive
221 to a combination of the bulk density, elastic thickness, and crustal thickness. Given that a precise
222 mapping of the crustal properties is limited by the uneven spatial resolution of the geodetic
223 measurements acquired by the MESSENGER mission, we use a spatio-spectral localization
224 approach to retrieve local information about Mercury's crust over regions that are well resolved in
225 our gravity solutions.
226 Localized correlations between gravity and topography were computed by Goossens et al. 2022
227 using a single taper for a spherical cap centered on each point of a 5°×5° latitude-longitude grid.
228 The resulting mapping of the average correlations for each local spectrum was carried out to
229 identify the regions with the highest correlations between gravity and topography. Four local areas
230 were selected to investigate the properties of the crust and lithosphere by using the measured
231 gravity/topography admittance (Goossens et al. 2022). In this study, we carried out local

admittance analyses on each point of $1^{\circ} \times 1^{\circ}$ grid investigating a total of 32,400 areas. For each spherical cap, we conducted gravity/topography localized spectral analyses, determining the localized spectral admittance $Z_M(l) = \frac{S_{hg}(l)}{S_{hh}(l)}$ and correlation $\gamma_M(l) = \frac{S_{hg}(l)}{\sqrt{S_{hh}(l) S_{gg}(l)}}$ (Wieczorek and Simons 2005). The cross- $\left(S_{gh}(l) = \sum_{m=0}^{l} g_{lm} h_{lm}\right)$ and auto-power spectra $\left(S_{gg}(l) = \sum_{m=0}^{l} g_{lm} g_{lm} \; and \; S_{hh}(l) = \sum_{m=0}^{l} h_{lm} h_{lm}\right)$ are computed using the measured localized topography (h_{lm}) and gravity (g_{lm}) that is upward/downward continued from the reference value R to the mean surface radius over the localized area. To account for the local resolution of the gravity field, we performed different localized spectral analyses by assuming spherical cap radii, θ, from 10° to 25° (step size of 1°) and a single taper that has a concentration factor of 99.9%, which dictates the spectral bandwidth of the window L_{win}. For a cap radius of 10°, for example, the spectral bandwidth of the localization window L_{win} is 33, whereas for an angular radius of 20° the bandwidth is 16. The maximum degree of the spherical harmonic expansion l_{max} of the gravity field for each analysis is based on the average degree strength computed across the investigated region (l_{DS} from Figure S1). We noted that the resolution of the gravity field obtained through the degree strength technique might be a conservative estimate, since gravity and topography show high correlations beyond degree l_{DS} for several local analyses.

Following Wieczorek and Simons (2005, 2007), we only interpret the localized measured admittance and correlation for the degree range from L_{win} to $l_{max} - L_{win}$. For each location, we select the windowing (*i.e.*, radius of the spherical cap) that leads to the widest range of degrees with gravity/topography correlations larger than 0.9.

To determine the local properties of the crust and lithosphere, we compare the localized measured admittance spectrum to the one based on the modeling of the gravity field of top loads (Turcotte

et al. 1981). A spherical shell model assumption enables the computation of a linear transfer function $Z_T(l)$ (*i.e.*, theoretical admittance function) that ties the topographic relief to gravity in the spherical harmonic domain ($c_{lm} = Z_T(l)\ h_{lm}$). By accounting for the modeling of loads placed on the planetary surface, the global theoretical admittance function is given by:

$$Z_T(l) = 4\,\pi G \left(\frac{l+1}{2l+1}\right) \rho_c \left[1 - \left(1 - \frac{T_c}{R}\right)^{l+2} C_l^0\right] \tag{3}$$

where T_c is the crustal thickness, ρ_c is the bulk crustal density, G the gravitational constant, and C_l^0 is the degree of compensation at each spherical harmonic degree l defined as follows

$$C_l^0 = \left\{1 - \frac{3}{(2l+1)\bar{\rho}}\left[\rho_c + \left(\rho_m - \rho_c\right)\left(\frac{R-T_c}{R}\right)^l\right]\right\}\left\{\frac{g_m}{g_0} - \frac{1}{\xi^l g_0(\rho_m - \rho_c)} - \frac{3}{\bar{\rho}(2l+1)}\left[\left(\rho_m - \rho_c\right)\left(1 - \frac{T_c}{R}\right) + \rho_c\left(1 - \frac{T_c}{R}\right)^{l+2}\right]\right\}^{-1}. \tag{4}$$

This expression of the degree of compensation is based on Broquet and Wieczorek 2019 formulation with the assumption that the surface loading density is equal to the crustal density. The wavelength-dependent parameter,

$$\xi^l = -\frac{R_e^4[l(l+1)-1+\nu]}{Dn^3+2Dn^2+ET_eR^2n}, \tag{5}$$

depends on: the scalar coefficient $n = l(l+1) - 2$; the flexural rigidity $D = \frac{ET_e^3}{12(1-\upsilon^2)}$ that is a function of the Young's modulus E, the Poisson ratio υ, the elastic thickness, T_e and the crustal thickness, T_c; and the radius of elastic shell midpoint radius $R_e = R - \frac{1}{2}T_e$, where R is the mean radius of the planet.

Theoretical admittances are computed by the varying crustal thickness, crustal density, and elastic thickness within a range of plausible values (Table 1). We used standard values for the other parameters, including a Young's modulus E of 100 GPa and a Poisson ratio υ of 0.25 (e.g., Hauck et al. 2004), while acknowledging that different values of E could be used (e.g., Melosh 1977;

Klimczak 2015; Kay and Dombard 2019). Changing the Young's modulus, however, does not significantly affect our results.

Each synthetic gravity field based on the assumed theoretical model is directly computed through the linear transfer function (Eq. 3). An alternative approach is based on the determination of the lithospheric deflections by assuming the first-order mass sheet approximation, and the finite-amplitude formulation (Wieczorek and Phillips 1998) is then applied to determine the gravity signal associated with each layer (*e.g.*, Broquet and Wieczorek 2019). This technique is important for Mars, for example, to compensate long-wavelength topographic variations resulting from its rotational flattening and Tharsis bulge (*e.g.*, Grott and Wieczorek 2012; Broquet and Wieczorek 2019). For Mercury, the errors associated with the finite-amplitude corrections are negligible (see Figure 11 by Wieczorek 2015) since the topographic excursions are minor, and this additional step to compute the synthetic gravitational potential is not required.

A grid search approach is then implemented to explore the range of acceptable values for the parameters of interest, ρ_c, T_c, and T_e. Table 1 provides the boundaries of the adjusted parameters that are based on extremely high porosity and high-density end-member materials for the crust, and thin and thick layers for both the crust and lithosphere. We used Eq. 3 to generate 337,881 synthetic gravity models that result from all possible combinations of the estimated parameters. We then computed the localized admittance of these theoretical models that was then compared with the observed localized spectral admittance (Z_M). To quantify the goodness of fit between the model and observations, we computed the misfit root-mean-square (RMS) of the admittance profiles by using a similar method proposed by Broquet and Wieczorek 2019), as follows,

$$RMS_{misfit} = \sqrt{\frac{1}{l_{max}-L_{win}} \sum_{l=L_{win}}^{l_{max}} [Z_T(l, T_e, T_c, \rho_c) - Z_M(l)]^2}. \quad (6)$$

The range of degrees investigated in the admittance spectrum is $L_{win} < l < l_{max} - L_{win}$, where the correlations are larger than 0.816 that corresponds to a signal to noise ratio of 2 (*e.g.*, see Eq. 11 from Grott and Wieczorek 2012). To investigate a wider range of spherical harmonic degrees, we assumed that the maximum degree l_{max} is computed by summing l_{DS} and the L_{win} adopted in the local analysis. This assumption involves that the upper limit of the range of spherical harmonic degrees used in the inversion is exactly equal to the degree strength, l_{DS}. While in general we should only investigate degrees in the range $l_{DS} - L_{win}$, we found that often correlations are still high. By using $l_{max} = l_{DS} + L_{win}$, we can extend a wider range of harmonic degrees, which should improve the robustness of the estimated parameters. We only use this extension if correlations are sufficiently high since we choose our L_{win} based on correlations > 0.816.

We accepted all analyses where the misfit was less than a critical value. We made use of the RMS of the formal uncertainties of the local admittance, $\overline{\sigma} = \sqrt{\frac{1}{l_{max}-L_{win}} \sum_{l=L_{win}}^{l_{max}} \sigma^2(l)}$, where the admittance uncertainty $\sigma(l)$ is defined as:

$$\sigma^2(l) = \frac{S_{gg}(l)}{S_{hh}(l)} \frac{1-\gamma_M(l)^2}{2l}. \quad (7)$$

For each spherical cap, we select the theoretical models that fulfill the criterion $RMS_{misfit} < \overline{\sigma}$. The areas that provide a spectral admittance analysis in agreement with this requirement are only 230. This limited coverage of Mercury's surface is caused by non-uniform correlation and admittance spectra that may be related to gravity data inaccuracies. The large misfit for the admittance may also be related to the theoretical model based on top loads only (Turcotte et al. 1981). Local areas, as, for example, in the Northern Volcanic Plains (NVP), show uniform high correlations but the observed admittance does not fulfill the criterion $RMS_{misfit} < 1\text{-}\overline{\sigma}$ with the predictions computed by assuming top loads only (*e.g.*, Figure S12). Top and bottom loading

313 flexural models (Broquet and Wieczorek 2019), for example, may help to enhance the admittance
314 fit in those regions (Goossens et al., 2022). This theoretical model is discussed in Sec. 4 to validate
315 our estimates of the crustal density.
316 Figure S10 shows the histogram of the latitudinal distribution of the local analyses that are
317 accepted in this study, highlighting that 65% of these analyses are above 60°N where the resolution
318 of Mercury's gravity field is higher. Therefore, the size of the localization window decreases with
319 increasing latitudes, as shown in Figure S11.
320

321 # 3. Results

322 The local admittance analysis yields the synthetic gravity models that are statistically
323 consistent with the measured localized admittance spectrum. To constrain the parameters of
324 interest (ρ_c, T_c, and T_e), we study both the misfit function and the probability density distribution
325 resulting from the pool of down-selected theoretical models. The probability density distribution
326 is obtained with the theoretical models that fulfill the acceptance criterion $RMS_{misfit} < \overline{\sigma}$. For
327 each analysis, we determine our best estimate and its uncertainty of the investigated parameters
328 ($\hat{\rho}_c \pm \sigma_{\rho_c}$, $\hat{T}_c \pm \sigma_{T_c}$, $\hat{T}_e \pm \sigma_{T_e}$) as the mean value and one standard deviation (*i.e.*, 68.3%
329 confidence interval) of the distribution of each parameter. The RMS_{misfit} is also computed as
330 function of the parameters of interest to better understand their impact on the admittance fit. The
331 misfit curves show the value that yields the best admittance fit (*i.e.*, minimum RMS_{misfit}). All the
332 solutions presented in this study provide mean values of the probability density distribution and
333 best fitting values that are fully consistent.
334 A statistical analysis of the inversion is obtained by investigating the probability density
335 distribution and the resulting uncertainty. Parameters that lead to approximately uniform

distributions are considered unconstrained by the local analysis. The model inversion enables the estimation of at least one parameter, showing a probability density distribution that resembles a Gaussian function.

Our local admittance analyses that provide information on Mercury's crust and lithosphere cover different areas in the northern hemisphere, including the High-Mg region, Northern Volcanic Plains (NVP), and Intercrater Plains (IcP). In Sections 3.1, 3.2 and 3.3, we present representative results of our admittance analyses for each region of interest. The results of the 230 analyses accepted in this study are archived on the Sapienza Space Robotics Investigation Group (SPRING) website.

3.1 High-Mg Region

Mercury's surface is Mg-rich compared to other terrestrial planets and lunar composition. The X-Ray Spectrometer (XRS) instrument onboard the MESSENGER spacecraft (Schlemm et al. 2007) enabled an accurate mapping of elemental abundances, including Mg/Si and Al/Si (Weider et al. 2015). A geochemical province with a high Mg/Si ratio was detected across the IcP. High gravity/topography correlations are observed over those terrains, and the measured admittance spectra fit the predictions based on synthetic gravity models that account for top-loading only. Figure 3-b shows correlation and admittance spectra between gravity and topography localized on a spherical cap centered at 286°E longitude and 44°N latitude with a localization window of 18°-radius and a concentration factor of 99.9%, resulting in a $L_{win} = 18$. The correlations are larger than 0.816 (*i.e.*, signal-to-noise ratio = 2) for the entire range of investigated degrees. The best fitting predicted admittance is constantly within 1-σ of the observed admittance. The resulting parameters of interest after the inversion are reported in Figure 4, which displays the misfit function and the probability density distributions. This local analysis allows us to constrain the

crustal density and elastic thickness that resemble a Gaussian distribution. The estimated crustal density and elastic thickness are $\hat{\rho}_c = 2597 \pm 67$ kg m^{-3} and $\hat{T}_e = 29 \pm 6$ km, respectively. Our models favor a crust thinner than 80 km with a high uncertainty (~23 km). These estimates are fully consistent with the analysis on the local area 1 presented by Goossens et al. 2022, which significantly overlaps with our investigated region. However, our admittance fit is based on top loads only, whereas the results by Goossens et al. 2022 are consistent with a positive loading parameter.

The localization window used to investigate this area is consistent with the geochemical boundaries of the High-Mg region. To further test and validate our results, we considered larger spherical caps for the spatio-spectral windowing. Figure S13 shows that the correlations decrease with increasing θ, suggesting that the measured gravity signal is associated with the geochemical properties of those terrains. Other local analyses across the High-Mg region are accepted in our study, providing consistent results and confirming that the estimated parameters correlate with the properties of that area.

3.2 Northern Volcanic Plains

The different content of Mg in Mercury's surface material also led to the identification of two geochemical provinces in the NVP (Weider et al. 2012). A lower abundance of Mg was observed at latitudes higher than 60°N compared to lower latitudes where Mg/Si ratios exceed 0.47 (Namur et al. 2016; Weider et al. 2015). To investigate these chemically different areas, we computed localized correlation and admittance in two regions that cover these provinces in the NVP.

Figure 5-b shows measured and predicted admittances retrieved after the localization of both gravity and topography fields on a 10°-radius spherical cap located over a region of the NVP

characterized by high-Mg abundances (*i.e.*, spherical cap center at $4°E$-longitude and $53°N$-latitude). The degree strength map indicates that the resolution of Mercury's gravity field is l_{DS}=115. The spectrum shows a drop in correlation at degree 78 (Figure 5-b), as expected, since it is close to $l_{DS} - L_{win}$, where $L_{win} = 33$ results from a concentration factor of 99.9%. This local analysis enables the accurate estimation of only the crustal density. The bulk density retrieved from the probability density distribution shown in Figure 6-d is $\hat{\rho}_c = 2595 \pm 33$ kg m^{-3}. This estimate is consistent with the densities that we measured in the High-Mg region across the IcP (Section 3.1). The gravity observed in this province of the NVP do not provide any constraint on the crustal thickness variations since all considered values are equally probable (Figure 6-b). In addition, no significant information is obtained for the elastic thickness, whose lower values ($T_e <$ 60 km), however, prevent from a good fit between measured and predicted admittances (Figure 6-c and -f).

The geochemical province characterized by low-Mg abundances cover a wide region of the NVP, including the edge between lightly cratered and heavily cratered terrains. By using a localization window of $\theta = 10°$ and a concentration factor of 99.9% for a spherical cap centered on $303°E$-longitude and $70°N$-latitude, high correlations are observed for a wide range of degrees (Figure 7-b) beyond $l_{DS} - L_{win}$, where l_{DS} is 102 accordingly to the degree strength map (Figure S1). Predicted and measured admittances agree within 1-σ, yielding constraints on the crust bulk density and the elastic thickness. Our measurements confirm that the crustal density across this region is lower ($\hat{\rho}_c = 2310 \pm 52$ kg m^{-3}) compared to the High-Mg province, as expected over regions with a low abundance of Mg across the NVP-IcP boundary. The estimated elastic thickness, 27 ± 18 km, is highly uncertain, suggesting a thinner lithosphere in this area (Figure 8-

c and -f). Crustal thickness is undetermined since the probability density distribution drops at large values (Figure 8-b and -e).

3.3 Intercrater Plains

A better understanding of the properties of the upper crust that formed during the Tolstojan era may be obtained through the investigation of local areas across the IcP (Denevi et al. 2018). Mercury was globally resurfaced, and these geological units were significantly affected by erosion, impacts and volcanism (*e.g.*, Fassett et al. 2011; Strom et al. 2011; Marchi et al. 2013). The IcP were defined after the Mariner 10 mission as gently rolling terrains with high density of superposed craters 5-10 km in diameter (Trask and Guest 1975). To constrain the mechanisms that led to the formation of the plains deposits that buried pre-existing impact craters, our local admittance analyses provide measurements of bulk density, crustal and elastic thickness across IcP on the eastside of Near Jokai and on the westside surrounding of the Caloris basin.

By localizing gravity and topography on a spherical cap centered on $250°E$-longitude and $72°N$-latitude with a radius $\theta = 15°$ and a windowing concentration factor of 99.9% ($L_{win} = 22$), a signal-to-noise ratio larger than 2 (*i.e.*, correlations > 0.816) is retrieved for a range of 30 degrees (Figure 9-b). Our fit of the measured and predicted admittances yields an accurate recovery of the crustal density only. Both crustal and elastic thicknesses show uniform distributions (Figure 10-e and -f). The probability density distribution obtained for the crustal density leads to $\hat{\rho}_c = 2487 \pm 39$ kg m^{-3}. The lateral variations of the crustal density between the High-Mg region and the IcP observed from our localized admittance studies is consistent with the computed grain densities (Beuthe et al. 2020).

The IcP mainly cover lower latitudes of Mercury's northern hemisphere where the resolution of the gravity field is limited. A strong contribution of the lithospheric flexure and crustal thickness to the measured field is expected for the lower spherical harmonic degrees. By investigating a region of the IcP on the westside surrounding of the Caloris basin, we used a localization window concentrated (99.9%) within a 25°-radius spherical cap ($L_{win} = 13$) that is centered at $110°E$-longitude and $38°N$-latitude. Figure 11-a shows the gravity anomalies within the spherical cap that shows their good correlation with the shaded topographic relief. Correlations are larger than 0.816 for the entire range of spherical harmonic degrees between L_{win} and $l_{DS} - L_{win}$. The predicted admittance spectra fit our measurements (Figure 11-b), allowing to constrain the crustal and elastic thicknesses in this region. The estimated crustal thickness $\hat{T}_c = 60 \pm 13$ km is in agreement with the retrieved mean value (~50 km) based on the inversion of the free-air gravity anomalies (Beuthe et al. 2020). A very thin lithosphere ($\hat{T}_c = 5 \pm 4$) is compatible with our admittance fit. However, the crustal density is undetermined, showing a quite uniform distribution (Figure 12-d). This result confirms that the gravity, because of its lower resolution over the analyzed local area, is poorly sensitive to the effects of crustal density variations. This local analysis is one of the cases that are not included in our next step to map out the lateral variations of the bulk density.

4. Discussion

An enhanced knowledge of the lateral variations of the properties of Mercury's crust and lithosphere is obtained through the combination of the parameters adjusted in our localized admittance studies. Before proceeding to map out our estimates across the northern hemisphere, we investigate a possible impact of bottom loads on our results (Section 4.1). Maps of the bulk density, and crust and elastic thicknesses are then generated to investigate their regional variations

449 (Section 4.2). By comparing our mapped bulk density with the grain density (Beuthe et al. 2020),
450 we then compute the surface porosity (Section 4.3).

451 4.1 Admittance Analysis with Bottom Loads

452 The theoretical model that is used in our study accounts for the presence of top loads only.
453 This modeling enables the estimation of three parameters (*i.e.,* ρ_c, T_c, T_e) through the admittance
454 fit. We carried out 32,400 correlation and admittance analyses across the northern hemisphere, and
455 this simplified model allowed us to limit the computational efforts in our grid search algorithm
456 (see Section 2.3). However, the existence of bottom loads underneath Mercury's surface may
457 induce a measurable gravity signal. To include the effects associated with internal loads, Goossens
458 et al. 2022 adopted the admittance model presented by Grott and Wieczorek 2012. The linear
459 transfer function for this approach relies on a set of parameters, including crustal density (ρ_c), load
460 density (ρ_l), loading parameter (L), crustal thickness (T_c), and elastic thickness (T_e). Surface and
461 internal loads are modeled by infinitesimally thin mass sheets and are assumed to be in phase (*e.g.*,
462 Broquet and Wieczorek 2019). This assumption is well-suited for bottom loads that are expected
463 to be below top loads, as, for example, for Mars' volcanic provinces (*e.g.*, Grott and Wieczorek
464 2012; Broquet and Wieczorek 2019). The four local areas investigated by Goossens et al. 2022 are
465 assumed to fulfill the hypothesis that top and bottom loads are in-phase. This assumption, however,
466 may not be valid for the entire northern hemisphere investigated in our study.

467 To determine if the local admittance analyses presented in Sec. 3 are significantly affected by
468 neglecting the effects of internal loads, we implemented the theoretical model presented by Grott
469 and Wieczorek 2012. We also modified the degree of compensation function to account for the
470 differences between crustal and load density accordingly to the formulation presented in the
471 Appendix B of the work by Broquet and Wieczorek 2019. Table S1 shows the bounds on the

parameters that we used to fit the measured admittance with the top/bottom loading model. By exploring a wide range of five parameter values ($i.e.$, $\rho_c, \rho_l, L, T_c, T_e$), we computed ~1M predicted admittance spectra for each local analysis. Admittance misfits were then retrieved to yield the estimation of the parameters of interest, as described in Sec. 2.3.

This theoretical model involves only surface loading for $L = 0$, and internal loading cases for $L \neq 0$. By exploring the space of this parameter, we investigate the impact of internal loading in our admittance fit. A positive loading parameter provides a positive density contrast that is assumed to be located at the base of the crust. A negative loading parameter accounts for the scenarios with subsurface and surface loads with opposite signs, and we assumed that the load is sufficiently deep in the upper mantle (160 km).

Figures S14-S23 show correlation and admittance spectra and the histograms for the parameters estimated in our analysis for the five areas presented in Sec. 3. By comparing these results with our solutions based on surface loads modeling, we note in general that the predicted fields that account for bottom loads lead to lower RMS_{misfit}. The first four cases are fully consistent with the results obtained with the admittance fit based on surface loads only (Figures 4d, 6d, 8d, and 10d). These local admittance analyses show that the best estimate of the loading parameter is L=0, supporting that the surface load modeling is fully adequate to predict the gravity signal. Furthermore, the probability distributions of the load density retrieved with the admittance analysis based on this theoretical model fully agree with the estimated crustal density with top loads only.

The presence of bottom loads, however, has a significant impact on the resulting probability distribution of the crustal and elastic thickness. The analysis localized on a spherical cap centered on 110ºE longitude and 38ºN latitude shows that bottom loads may not be excluded (Figure S23),

and the resulting T_c and T_e estimates significantly differ from the case with top loads only. This occurs for the cases where the bulk density is undetermined, since the resolution of the gravity field is lower.

In this study, we mainly focus on the lateral variations of the bulk density that is estimated from the admittance analyses based on top loads only. Maps of crustal and elastic thickness are also generated and reported in the supplementary material, but the assumption of a theoretical model with top loads may significantly affect their accuracy over local areas where bottom loading should be accounted for.

4.2 Lateral Variations of the Bulk Density

The estimates of the bulk density, crustal thickness and elastic thickness carried out with the 230 localized admittance analyses presented in Sec. 3 are then used to map out the properties of the crust across the northern hemisphere. The local estimate of these parameters is representative of their mean value within the spherical cap. To map out the lateral variations of these parameters on a 1°×1°grid, we account for the estimated value and its uncertainty resulting from each local analysis that covers a specific point on the grid. By averaging out these values on each grid point, we retrieve a map of the bulk density, and crustal and elastic thicknesses with their uncertainties. The left panel of Figure 13 shows the measured regional variations of the crust bulk density in the northern hemisphere. Areas left blank in the maps do not provide measured spectra that are consistent with predictions (RMS_{misfit} >1-$\bar{\sigma}$) or the parameter of interest shows a uniform probability density distribution.

We determined an average bulk density of 2540 ± 61 kg m^{-3} in the observed area of the northern hemisphere. Significant lateral variations are detected across the edge between the NVP and the

high-Mg province, where modeling of the surface mineralogy suggest a higher abundance of forsterite (Namur and Charlier 2017). A high abundance of Mg is consistent with the observed larger crustal density ($\sim 2550\ kg\ m^{-3}$), which is, however, significantly lower compared to the calculated grain density (Sori 2018; Beuthe et al. 2020). This result is explained by the presence of surface porosity. The right panel of Figure 13 shows the map of the formal uncertainty of the bulk crustal density. Lower uncertainties are retrieved at higher latitudes where MESSENGER enabled the acquisition of radio tracking data at low altitudes ($< 50\ km$).

Maps of crustal and elastic thicknesses are also generated to show their lateral variations (Figures S14 and S15). The crustal thickness is accurately estimated only over a north-west region of the NVP with an uncertainty lower than 10 km (Figure S14). The high-Mg province and the IcP show crustal thickness uncertainties of 10-20 km. A mean estimate of the crustal thickness constrained in the observed northern hemisphere is $29.9 \pm 15\ km$, which is in full agreement with previous independent estimates (e.g., Padovan et al. 2015). The lithosphere also provides a significant contribution to the gravity signal measured by MESSENGER, and this parameter is constrained through the local admittance analyses. The left panel of Figure S15 shows a thicker lithosphere (30 ± 10 km) across regions with a number of craters $N(D) > 150$ with diameter $D > 20$ km per million km^2 (*e.g.*, Fassett et al. 2011; Denevi et al. 2018), including the high-Mg province. A thinner lithosphere is noted in the NVP and in the IcP on the westside region of the Caloris basin. Our estimated mean elastic thickness is 12.4 ± 6.3 km. The lateral variations of the crustal and elastic thickness may be affected by our assumption that the theoretical modeling is based on top loads only.

4.3 Surface Porosity

Gravity measurements provide constraints on the mean bulk density of Mercury's crust. Independent estimates of the lateral variations in density of the pore-free surface rocks (grain density) were obtained through a combination of geochemical data acquired by the MESSENGER XRS instrument (Schlemm et al. 2007) and mineral proportions obtained from laboratory crystallization experiments (Namur and Charlier 2017; Beuthe et al. 2020). Our estimates of the bulk density are, as expected, lower compared to the grain density retrieved from global mineralogical mapping. The estimated bulk density varies between 2350 and 2650 kg m^{-3}, whereas the calculated grain density is in a 2750-3150 kg m^{-3} range.

Porosity induced by impact cratering can be determined by comparing gravity and mineralogical estimates. The presence of graphite (with a density of about 2200 kg m^{-3}) in the crust (Peplowski et al. 2016) might also be partly responsible for the difference between grain density calculated from surface mineralogy (that excluded graphite) and bulk density obtained from gravity. However, graphite concentrations are estimated to be low, around 1–5 wt% (Murchie et al. 2015), with maximum values in low-reflectance materials that are excavated deeper in the crust (Klima et al. 2018). Such concentrations have a negligible effect on grain density.

By assuming that Mercury's surface composition is representative of the outer layers of the crust, the porosity ϕ is computed locally by using the bulk density ($\bar{\rho}_c$) from gravity and the grain density (ρ_g) from mineralogy through the following formula

$$\phi = 1 - \frac{\bar{\rho}_c}{\rho_g}. \quad (9)$$

The left panel of Figure 14-a shows the local variations of the crustal porosity with a maximum value of ~21%, which results from the range of the measured pore-free surface rocks. Our estimates over the observed northern hemisphere suggest a mean value of $14.7 \pm 1.6\%$, which is larger than Moon's crustal porosity that is on average 12% (Wieczorek et al. 2013). High relative

562 global impact fluxes and mean velocity of the impacting projectiles on Mercury (Le Feuvre and
563 Wieczorek 2008) could potentially contribute to higher crustal porosities on Mercury than the
564 Moon.
565 High crustal porosities are observed across heavily cratered regions. Impact events fracture the
566 crust, yielding the generation of additional pore space (Reynolds 1885). A longer history of
567 bombardment generally results in higher porosity. Low porosities are detected across the NVP,
568 where impact bombardments after their formation ~4 Gy ago strongly affected their bulk density
569 (Frank et al. 2017; Whitten et al. 2014). A region located within $210-240°E$ longitudes and $60-$
570 $80°N$ latitudes that is characterized by high crater densities (*i.e.*, *N(20)* >150 per million km^2)
571 shows 10% porosities. Preexisting high porosity in the crust across this heavily cratered province
572 may have led to the compaction of the pore space for some impacts, which may lead to equilibrium
573 porosity after sufficient bombardment (Milbury et al. 2015).

574 ## 5. Conclusions

575 The enhanced spatial resolution of Mercury's gravity field *HgM009* allowed us to study the
576 properties of the crust and lithosphere by using localized spectral admittance analyses. Compared
577 to the accuracy of other celestial bodies' gravity field, as, for example, the Moon and Mars, our
578 knowledge of the short wavelength anomalies is still limited to a few regions of the northern
579 hemisphere. The resolution of the gravity field is between spherical harmonic degrees 80 and 160
580 across the mid-northern latitudes. The gravity signal associated with those harmonics is caused by
581 different sources, including the crustal density and thickness variations, and the flexure of the
582 lithosphere.
583 To estimate the crust and lithospheric properties, we used a method that uses the combination of
584 localized admittance spectra and predictions based on a lithospheric flexural model (Turcotte et al.

585 1981). The crustal density and thickness, and the elastic thickness are adjusted as free parameters
586 to obtain a good fit between the measured and predicted spectra. Crustal thickness variations that
587 are not associated with flexure are not included in our modeling, limiting our interpretation
588 regarding local variations of the crustal thickness. The parameter that is best constrained in our
589 analysis is the bulk density, and a map of its lateral variations (Figure 13) provides key information
590 on the crustal porosity (Figure 14).
591 An accurate fit between measured and predicted admittance spectra is obtained across a few
592 regions of Mercury's northern hemisphere, including the high-Mg province, the NVP, and the IcP.
593 This may result from the resolution of the gravity field that is still limited at lower latitudes.
594 Furthermore, the theoretical model adopted in our study accounts for top-loading only. Surface
595 and subsurface load modeling (e.g., Grott and Wieczorek 2012; Broquet and Wieczorek 2019)
596 may help to enhance the admittance fit between measurements and predictions. This transfer
597 function, however, is often based on the assumption that the ratio of surface to subsurface loads is
598 constant for all degrees (*e.g.*, Broquet and Wieczorek 2019), which would not be well-suited for
599 the entire northern hemisphere.
600 The map of the bulk density is combined with the map of the grain density (Namur and Charlier
601 2017; Beuthe et al. 2020) to yield the lateral variations of the upper crust porosity. Higher crustal
602 porosities are observed across the high-Mg region.
603 To investigate the crust and lithosphere in the southern hemisphere, accurate measurements of
604 gravity and topography will be acquired by the ESA mission BepiColombo that will be orbiting
605 Mercury from December 2025 (Genova et al. 2021). Mercury's gravity field will be estimated
606 globally to spherical harmonics degree and order 50-60. The method proposed in this study will

607 then be used to analyze gravity/topography admittance spectra, enabling geophysical constraints
608 on the properties of the crust in the southern hemisphere.
609

610 Acknowledgements

611 The gravity field *HgM009* and the ancillary information, including the covariance matrix,
612 presented in this study are archived at https://sites.google.com/uniroma1.it/spring. Our software
613 that enables localized spectral analyses of gravity/topography correlation and admittance is based
614 on the free software package *shtools* (Wieczorek and Meschede 2018). We are grateful to Walter
615 S. Kiefer and an anonymous reviewer for helpful and constructive comments on previous versions
616 of this paper. AG acknowledges funding from the *Rita Levi Montalcini Programme* of the Italian
617 Ministry of University and Research (MUR).

References

Becker, Kris J, Mark S Robinson, Tammy L Becker, Lynn A Weller, Kenneth L Edmundson, Gregory A Neumann, Mark E Perry, and Sean C Solomon. 2016. "First Global Digital Elevation Model of Mercury." In *Presented at the 47th Lunar and Planetary Science Conference*. Houston, TX: Lunar and Planetary Institute.

Beuthe, Mikael, Bernard Charlier, Olivier Namur, Attilio Rivoldini, and Tim van Hoolst. 2020. "Mercury's Crustal Thickness Correlates With Lateral Variations in Mantle Melt Production." *Geophysical Research Letters* 47 (9): e2020GL087261. https://doi.org/10.1029/2020GL087261.

Broquet, A., and M. A. Wieczorek. 2019. "The Gravitational Signature of Martian Volcanoes." *Journal of Geophysical Research: Planets* 124 (8): 2054–86. https://doi.org/10.1029/2019JE005959.

Byrne, Paul K., Lillian R. Ostrach, Caleb I. Fassett, Clark R. Chapman, Brett W. Denevi, Alexander J. Evans, Christian Klimczak, Maria E. Banks, James W. Head, and Sean C. Solomon. 2016. "Widespread Effusive Volcanism on Mercury Likely Ended by about 3.5 Ga." *Geophysical Research Letters* 43 (14): 7408–16. https://doi.org/10.1002/2016GL069412.

Charlier, Bernard, Timothy L. Grove, and Maria T. Zuber. 2013. "Phase Equilibria of Ultramafic Compositions on Mercury and the Origin of the Compositional Dichotomy." *Earth and Planetary Science Letters* 363 (February): 50–60. https://doi.org/10.1016/J.EPSL.2012.12.021.

Charlier, Bernard, and Olivier Namur. 2019. "The Origin and Differentiation of Planet Mercury." *Elements* 15 (1): 9–14. https://doi.org/10.2138/GSELEMENTS.15.1.9.

Denevi, B.W., C.M. Ernst, L.M. Prockter, and M.S. Robinson. 2018. "The Geologic History of Mercury'." In *Mercury*, edited by Sean C. Solomon, Larry R. Nittler, and Brian J. Anderson, 144–75. Cambridge University Press (2018). https://doi.org/10.1017/9781316650684.

Ermakov, A. I., R. S. Park, and B. G. Bills. 2018. "Power Laws of Topography and Gravity Spectra of the Solar System Bodies." *Journal of Geophysical Research: Planets* 123 (8): 2038–64. https://doi.org/10.1029/2018JE005562.

Fassett, C I, S J Kadish, J W Head, S C Solomon, and R G Strom. 2011. "The Global Population of Large Craters on Mercury and Comparison with the Moon." *Wiley Online Library* 38 (10): 10202. https://doi.org/10.1029/2011GL047294.

Frank, Elizabeth A., Ross W.K. Potter, Oleg Abramov, Peter B. James, Rachel L. Klima, Stephen J. Mojzsis, and Larry R. Nittler. 2017. "Evaluating an Impact Origin for Mercury's High-Magnesium Region." *Journal of Geophysical Research: Planets* 122 (3): 614–32. https://doi.org/10.1002/2016JE005244.

Genova, A., S. Goossens, E. Mazarico, F.G. Lemoine, G.A. Neumann, W. Kuang, T.J. Sabaka, et al. 2019. "Geodetic Evidence That Mercury Has A Solid Inner Core." *Geophysical Research Letters* 46 (7). https://doi.org/10.1029/2018GL081135.

Genova, A., L. Iess, and M. Marabucci. 2013. "Mercury's Gravity Field from the First Six Months of MESSENGER Data." *Planetary and Space Science* 81 (June): 55–64. https://doi.org/10.1016/J.PSS.2013.02.006.

Genova, A., E. Mazarico, S. Goossens, F.G. Lemoine, G.A. Neumann, D.E. Smith, and M.T. Zuber. 2018. "Solar System Expansion and Strong Equivalence Principle as Seen by the

NASA MESSENGER Mission." *Nature Communications* 9 (1). https://doi.org/10.1038/s41467-017-02558-1.

Genova, Antonio, Hauke Hussmann, Tim Van Hoolst, Daniel Heyner, Luciano Iess, Francesco Santoli, Nicolas Thomas, et al. 2021. "Geodesy, Geophysics and Fundamental Physics Investigations of the BepiColombo Mission." *Space Science Reviews 2021 217:2* 217 (2): 1–62. https://doi.org/10.1007/S11214-021-00808-9.

Goossens, S., A. Genova, P. B. James, and E. Mazarico. 2022. "Estimation of Crust and Lithospheric Properties for Mercury from High-resolution Gravity and Topography." *The Planetary Science Journal* 3(6): 145. https://doi.org/10.3847/PSJ/ac703f.

Goossens, S., T.J. Sabaka, A. Genova, E. Mazarico, J.B. Nicholas, and G.A. Neumann. 2017. "Evidence for a Low Bulk Crustal Density for Mars from Gravity and Topography." *Geophysical Research Letters* 44 (15). https://doi.org/10.1002/2017GL074172.

Grott, M., and M. A. Wieczorek. 2012. "Density and Lithospheric Structure at Tyrrhena Patera, Mars, from Gravity and Topography Data." *Icarus* 221 (1): 43–52. https://doi.org/10.1016/J.ICARUS.2012.07.008.

Hauck, Steven A., Andrew J. Dombard, Roger J. Phillips, and Sean C. Solomon. 2004. "Internal and Tectonic Evolution of Mercury." *Earth and Planetary Science Letters* 222 (3–4): 713–28. https://doi.org/10.1016/J.EPSL.2004.03.037.

James, Peter B., Maria T. Zuber, Roger J. Phillips, and Sean C. Solomon. 2015. "Support of Long-Wavelength Topography on Mercury Inferred from MESSENGER Measurements of Gravity and Topography." *Journal of Geophysical Research: Planets* 120 (2): 287–310. https://doi.org/10.1002/2014JE004713.

Kaula, W.M. 1966. *Theory of Satellite Geodesy. Applications of Satellites to Geodesy*. Waltham, MA: Blaisdell Publishing Company.

Kay, Jonathan P., and Andrew J. Dombard. 2019. "Long-Wavelength Topography on Mercury Is Not from Folding of the Lithosphere." *Icarus* 319 (February): 724–28. https://doi.org/10.1016/J.ICARUS.2018.09.040.

Klima, Rachel L., Brett W. Denevi, Carolyn M. Ernst, Scott L. Murchie, and Patrick N. Peplowski. 2018. "Global Distribution and Spectral Properties of Low-Reflectance Material on Mercury." *Geophysical Research Letters* 45 (7): 2945–53. https://doi.org/10.1002/2018GL077544.

Klimczak, Christian. 2015. "Limits on the Brittle Strength of Planetary Lithospheres Undergoing Global Contraction." *Journal of Geophysical Research: Planets* 120 (12): 2135–51. https://doi.org/10.1002/2015JE004851.

Konopliv, A. S., W. B. Banerdt, and W. L. Sjogren. 1999. "Venus Gravity: 180th Degree and Order Model." *Icarus* 139 (1): 3–18. https://doi.org/10.1006/ICAR.1999.6086.

Konopliv, A. S., R. S. Park, and A. I. Ermakov. 2020. "The Mercury Gravity Field, Orientation, Love Number, and Ephemeris from the MESSENGER Radiometric Tracking Data." *Icarus* 335 (January): 113386. https://doi.org/10.1016/J.ICARUS.2019.07.020.

Le Feuvre, M., and M.A. Wieczorek. 2008. "Nonuniform Cratering of the Terrestrial Planets." *Icarus* 197 (1): 291–306. https://doi.org/10.1016/J.ICARUS.2008.04.011.

Marchi, Simone, Clark R. Chapman, Caleb I. Fassett, James W. Head, W. F. Bottke, and Robert G. Strom. 2013. "Global Resurfacing of Mercury 4.0–4.1 Billion Years Ago by Heavy Bombardment and Volcanism." *Nature 2013 499:7456* 499 (7456): 59–61. https://doi.org/10.1038/nature12280.

Margot, Jean-Luc, Stanton J. Peale, Sean C. Solomon, Steven A. Hauck, Frank D. Ghigo, Raymond F. Jurgens, Marie Yseboodt, Jon D. Giorgini, Sebastiano Padovan, and Donald B. Campbell. 2012. "Mercury's Moment of Inertia from Spin and Gravity Data." *Journal of Geophysical Research: Planets* 117 (E12): 0–09. https://doi.org/10.1029/2012JE004161.

Mazarico, E., A. Genova, S. Goossens, F.G. Lemoine, G.A. Neumann, M.T. Zuber, D.E. Smith, and S.C. Solomon. 2014. "The Gravity Field, Orientation, and Ephemeris of Mercury from MESSENGER Observations after Three Years in Orbit." *Journal of Geophysical Research: Planets* 119 (12). https://doi.org/10.1002/2014JE004675.

Melosh, J.H. 1977. "Global Tectonics of a Despun Planet." *Icarus* 31 (2): 221–43. https://doi.org/10.1016/0019-1035(77)90035-5.

Milbury, C., B. C. Johnson, H. J. Melosh, G. S. Collins, D. M. Blair, J. M. Soderblom, F. Nimmo, C. J. Bierson, R. J. Phillips, and M. T. Zuber. 2015. "Preimpact Porosity Controls the Gravity Signature of Lunar Craters." *Geophysical Research Letters* 42 (22): 9711–16. https://doi.org/10.1002/2015GL066198.

Murchie, Scott L., Rachel L. Klima, Brett W. Denevi, Carolyn M. Ernst, Mary R. Keller, Deborah L. Domingue, David T. Blewett, et al. 2015. "Orbital Multispectral Mapping of Mercury with the MESSENGER Mercury Dual Imaging System: Evidence for the Origins of Plains Units and Low-Reflectance Material." *Icarus* 254 (July): 287–305. https://doi.org/10.1016/J.ICARUS.2015.03.027.

Namur, Olivier, and Bernard Charlier. 2017. "Silicate Mineralogy at the Surface of Mercury." https://doi.org/10.1038/NGEO2860.

Namur, Olivier, Max Collinet, Bernard Charlier, Timothy L. Grove, Francois Holtz, and Catherine McCammon. 2016. "Melting Processes and Mantle Sources of Lavas on Mercury." *Earth and Planetary Science Letters* 439 (April): 117–28. https://doi.org/10.1016/J.EPSL.2016.01.030.

Peplowski, Patrick N, Rachel L Klima, David J Lawrence, Carolyn M Ernst, Brett W Denevi, Elizabeth A Frank, John O Goldsten, Scott L Murchie, Larry R Nittler, and Sean C Solomon. 2016. "Remote Sensing Evidence for an Ancient Carbon-Bearing Crust on Mercury" 9: 273–76. https://doi.org/10.1038/NGEO2669.

Reynolds, Osborne. 1885. " LVII. On the Dilatancy of Media Composed of Rigid Particles in Contact. With Experimental Illustrations ." *The London, Edinburgh, and Dublin Philosophical Magazine and Journal of Science* 20 (127): 469–81. https://doi.org/10.1080/14786448508627791.

Schlemm, Charles E., Richard D. Starr, George C. Ho, Kathryn E. Bechtold, Sarah A. Hamilton, John D. Boldt, William V. Boynton, et al. 2007. "The X-Ray Spectrometer on the MESSENGER Spacecraft." *The Messenger Mission to Mercury*, 393–415. https://doi.org/10.1007/978-0-387-77214-1_11.

Smith, David E., Maria T. Zuber, Roger J. Phillips, Sean C. Solomon, Steven A. Hauck, Frank G. Lemoine, Erwan Mazarico, et al. 2012. "Gravity Field and Internal Structure of Mercury from MESSENGER." *Science* 336 (6078): 214–17. https://doi.org/10.1126/SCIENCE.1218809.

Solomon, Sean C., Ralph L. McNutt, Robert E. Gold, Mario H. Acuña, Daniel N. Baker, William V. Boynton, Clark R. Chapman, et al. 2001. "The MESSENGER Mission to Mercury: Scientific Objectives and Implementation." *Planetary and Space Science* 49 (14–15): 1445–65. https://doi.org/10.1016/S0032-0633(01)00085-X.

Solomon, Sean C., Larry R. Nittler, and Brian J. Anderson, eds. 2018. *Mercury: The View after MESSENGER*. Vol. 21. Cambridge, UK: Cambridge University Press.

Sori, Michael M. 2018. “A Thin, Dense Crust for Mercury.” *Earth and Planetary Science Letters* 489 (May): 92–99. https://doi.org/10.1016/J.EPSL.2018.02.033.

Strom, Robert G., Maria E. Banks, Clark R. Chapman, Caleb I. Fassett, Jeffrey A. Forde, James W. Head, William J. Merline, Louise M. Prockter, and Sean C. Solomon. 2011. “Mercury Crater Statistics from MESSENGER Flybys: Implications for Stratigraphy and Resurfacing History.” *Planetary and Space Science* 59 (15): 1960–67. https://doi.org/10.1016/J.PSS.2011.03.018.

Tapley, Byron D., Bob E. Schutz, and George H. Born. 2004. *Statistical Orbit Determination*. *Statistical Orbit Determination*. Elsevier Inc. https://doi.org/10.1016/B978-0-12-683630-1.X5019-X.

Trask, Newell J., and John E. Guest. 1975. “Preliminary Geologic Terrain Map of Mercury.” *Journal of Geophysical Research* 80 (17): 2461–77. https://doi.org/10.1029/JB080I017P02461.

Turcotte, D. L., R. J. Willemann, W. F. Haxby, and John Norberry. 1981. “Role of Membrane Stresses in the Support of Planetary Topography.” *Journal of Geophysical Research: Solid Earth* 86 (B5): 3951–59. https://doi.org/10.1029/JB086IB05P03951.

Vander Kaaden, Kathleen E., and Francis M. McCubbin. 2015. “Exotic Crust Formation on Mercury: Consequences of a Shallow, FeO-Poor Mantle.” *Journal of Geophysical Research: Planets* 120 (2): 195–209. https://doi.org/10.1002/2014JE004733.

Verma, Ashok Kumar, and Jean-Luc Margot. 2016. “Mercury’s Gravity, Tides, and Spin from MESSENGER Radio Science Data.” *Journal of Geophysical Research: Planets* 121 (9): 1627–40. https://doi.org/10.1002/2016JE005037.

Weider, Shoshana Z., Larry R. Nittler, Richard D. Starr, Ellen J. Crapster-Pregont, Patrick N. Peplowski, Brett W. Denevi, James W. Head, et al. 2015. “Evidence for Geochemical Terranes on Mercury: Global Mapping of Major Elements with MESSENGER’s X-Ray Spectrometer.” *Earth and Planetary Science Letters* 416 (April): 109–20. https://doi.org/10.1016/J.EPSL.2015.01.023.

Weider, Shoshana Z., Larry R. Nittler, Richard D. Starr, Timothy J. McCoy, Karen R. Stockstill-Cahill, Paul K. Byrne, Brett W. Denevi, James W. Head, and Sean C. Solomon. 2012. “Chemical Heterogeneity on Mercury’s Surface Revealed by the MESSENGER X-Ray Spectrometer.” *Journal of Geophysical Research: Planets* 117 (E12): 0–05. https://doi.org/10.1029/2012JE004153.

Whitten, Jennifer L., James W. Head, Brett W. Denevi, and Sean C. Solomon. 2014. “Intercrater Plains on Mercury: Insights into Unit Definition, Characterization, and Origin from MESSENGER Datasets.” *Icarus* 241 (October): 97–113. https://doi.org/10.1016/J.ICARUS.2014.06.013.

Wieczorek, Mark A. 2015. “The Gravity and Topography of the Terrestrial Planets.” In *Treatise on Geophysics*.

Wieczorek, Mark A., and Matthias Meschede. 2018. “SHTools: Tools for Working with Spherical Harmonics.” *Geochemistry, Geophysics, Geosystems* 19 (8): 2574–92. https://doi.org/10.1029/2018GC007529.

Wieczorek, Mark A., Gregory A. Neumann, Francis Nimmo, Walter S. Kiefer, G. Jeffrey Taylor, H. Jay Melosh, Roger J. Phillips, et al. 2013. “The Crust of the Moon as Seen by GRAIL.” *Science* 339 (6120): 671–75. https://doi.org/10.1126/SCIENCE.1231530.

Wieczorek, Mark A., and Frederik J. Simons. 2005. “Localized Spectral Analysis on the Sphere.” *Geophysical Journal International* 162 (3): 655–75. https://doi.org/10.1111/J.1365-246X.2005.02687.X/2/162-3-655-FIG011.JPEG.

Zuber, Maria T., David E. Smith, Roger J. Phillips, Sean C. Solomon, Gregory A. Neumann, Steven A. Hauck, Stanton J. Peale, et al. 2012. “Topography of the Northern Hemisphere of Mercury from MESSENGER Laser Altimetry.” *Science* 336 (6078): 217–20. https://doi.org/10.1126/SCIENCE.1218805.

Tables

Table 1 Lower and upper limits, and step size of the parameters of interest that are used in the global theoretical admittance function (Eqs. 3 and 4).

Parameter	Lower Bound	Upper Bound	Step Size
Crustal density ρ_c (kg m^{-3})	2200	3200	5
Crustal thickness T_c (km)	0	200	5
Elastic thickness T_e (km)	0	200	5

Figures

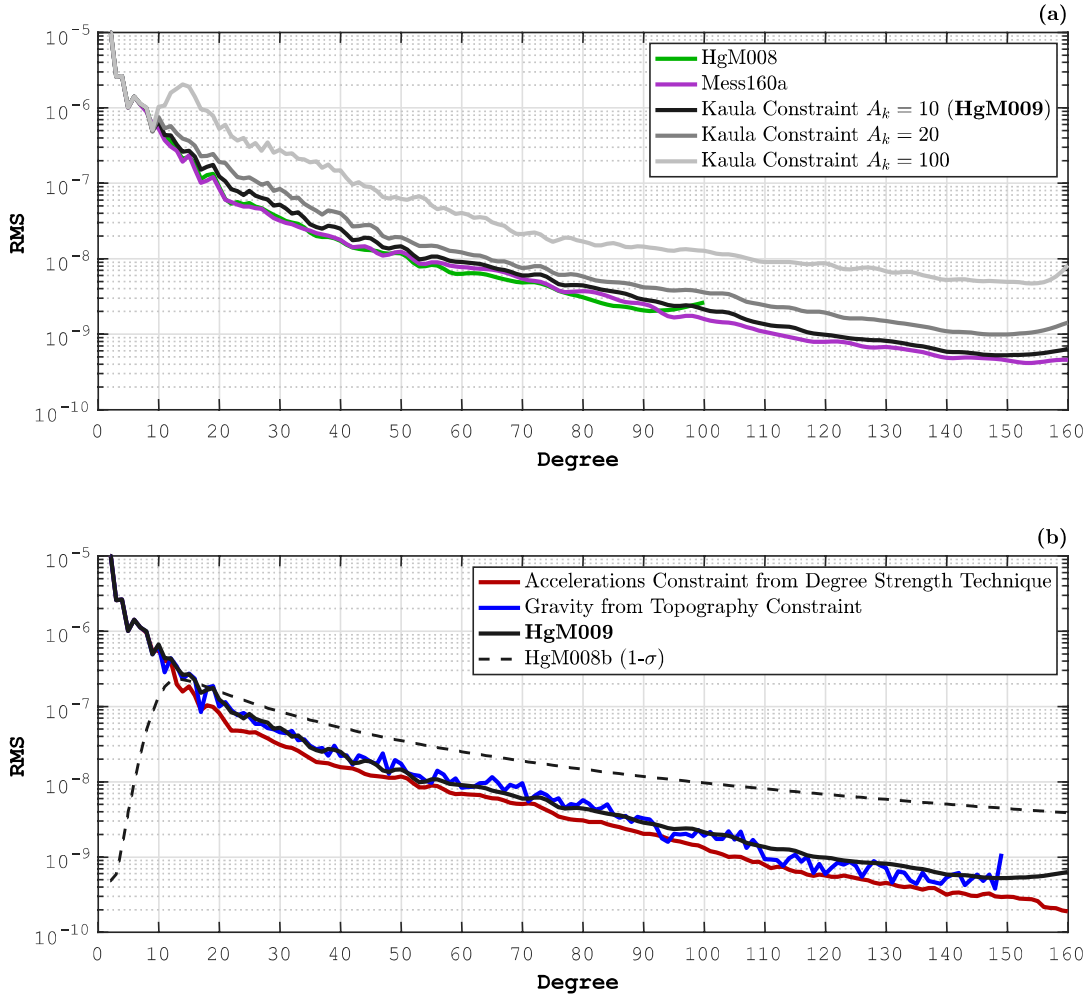

Figure 1 Power spectra of the gravity solutions obtained by using an *a priori* constraint based on (**a**) the Kaula rule with different A_k parameters and (**b**) the degree strength map (**red**) and the gravity from topography (**blue**). The gravity solution, *HgM009*, is expanded to degree and order 160 and is retrieved with a looser Kaula constraint (A_k=10) compared to the latest solutions *HgM008* (**green**) and *Mess160a* (**purple**).

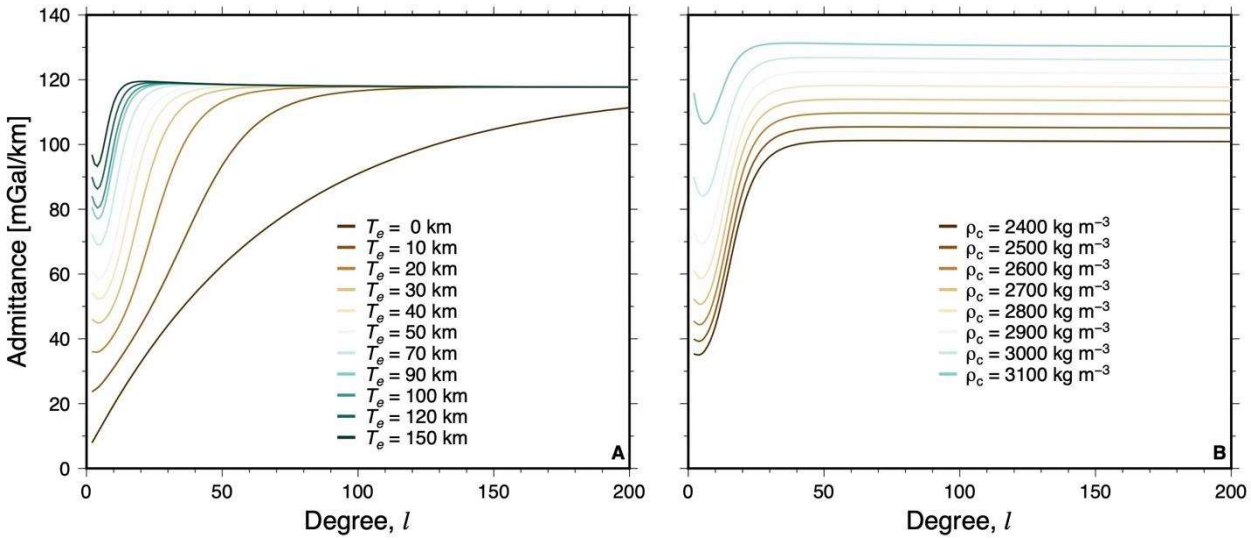

Figure 2 (**A**) Global gravity/topography admittances for crustal thickness and density of 35 km and 2800 kg m^{-3}, respectively. (**B**) Global gravity/topography admittances for crustal and elastic thickness of 35 km and 50 km, respectively.

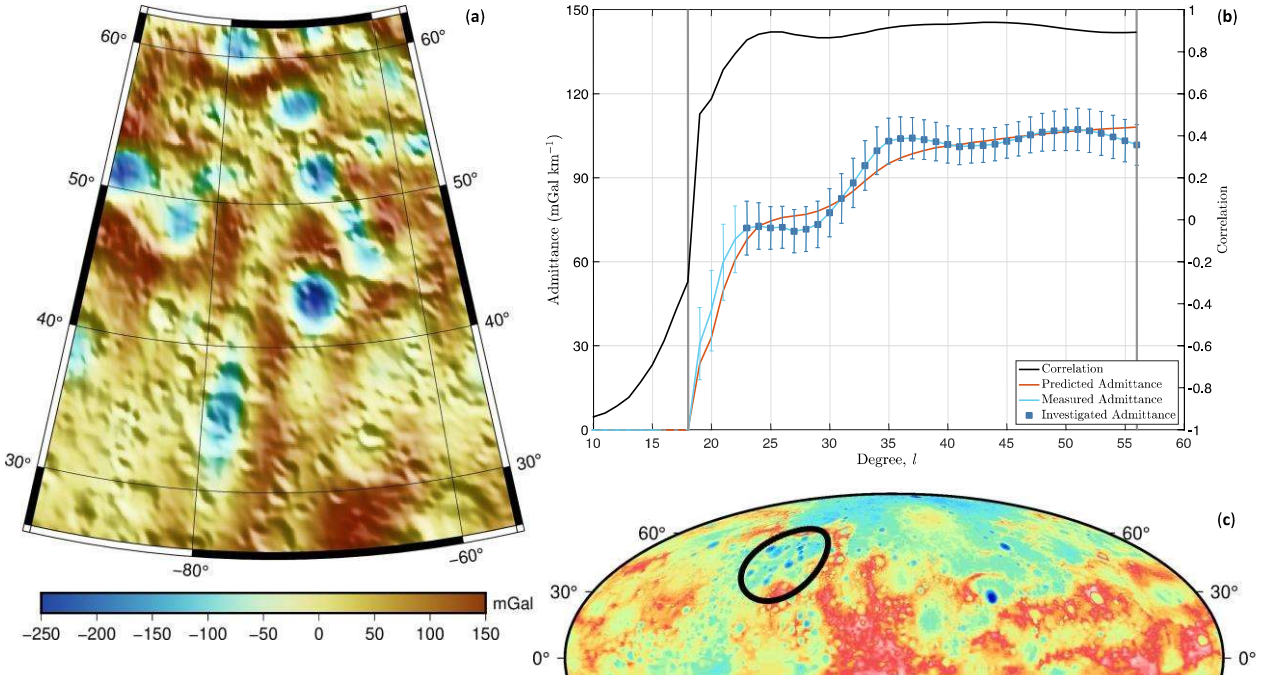

Figure 3 (**a**) Local map of free-air gravity anomaly (mGal) shown over shaded topographic relief in a Lambert Conformal Conic projection, and (**b**) correlation and admittance between gravity and topography localized on (**c**) a spherical cap centered at 286°E longitude and 44°N latitude. The localization windowing is carried out with a 18° radius, a concentration factor of 0.999 ($L_{win} = 18$), and a spherical harmonic expansion to degree $l_{max} = 74$. The measured admittance is compared to the predicted admittance spectra based on the surface loading model presented in Sec. 2.3. The investigated admittance spectrum includes spherical harmonic degrees that provides a signal to noise ratio larger than (correlation $\gamma(l)$>0.816). The vertical gray lines show the range of spherical harmonic degrees between L_{win} and $l_{max} - L_{win} = l_{DS}$, where l_{DS} is the degree resolution resulting from the degree strength map (Figure S1).

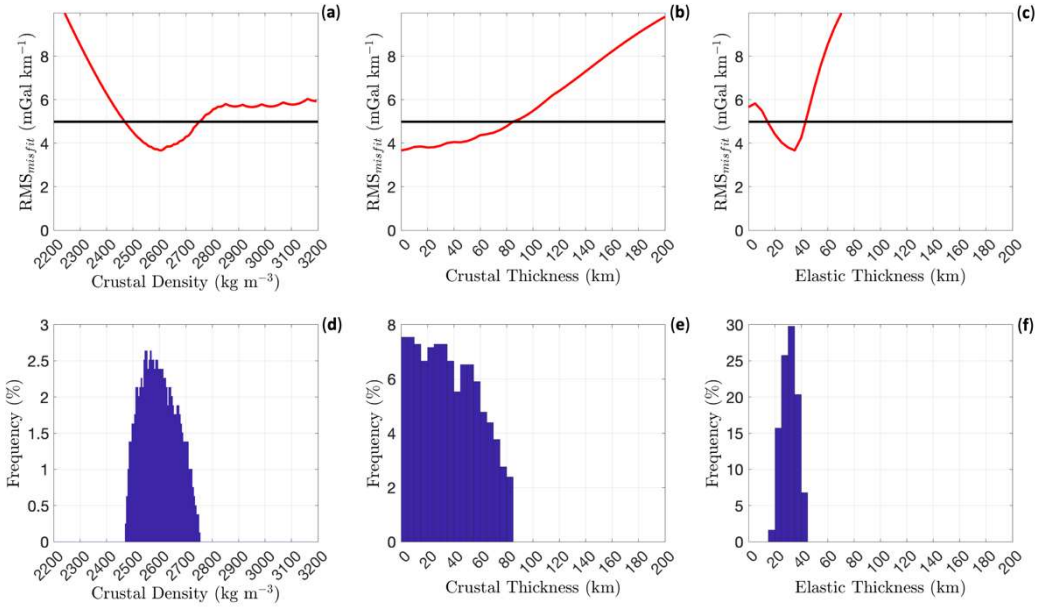

Figure 4 (**a-b-c**) Misfit plots and (**d-e-f**) histograms for the crustal density and thickness, and elastic thickness resulting from the comparison between measured and predicted localized admittance shown in Figure 3-b. The black horizontal line shows the RMS of the formal uncertainties of the local admittance, $\overline{\sigma}$, and the red curve the RMS_{misfit}as function of the estimated parameter.

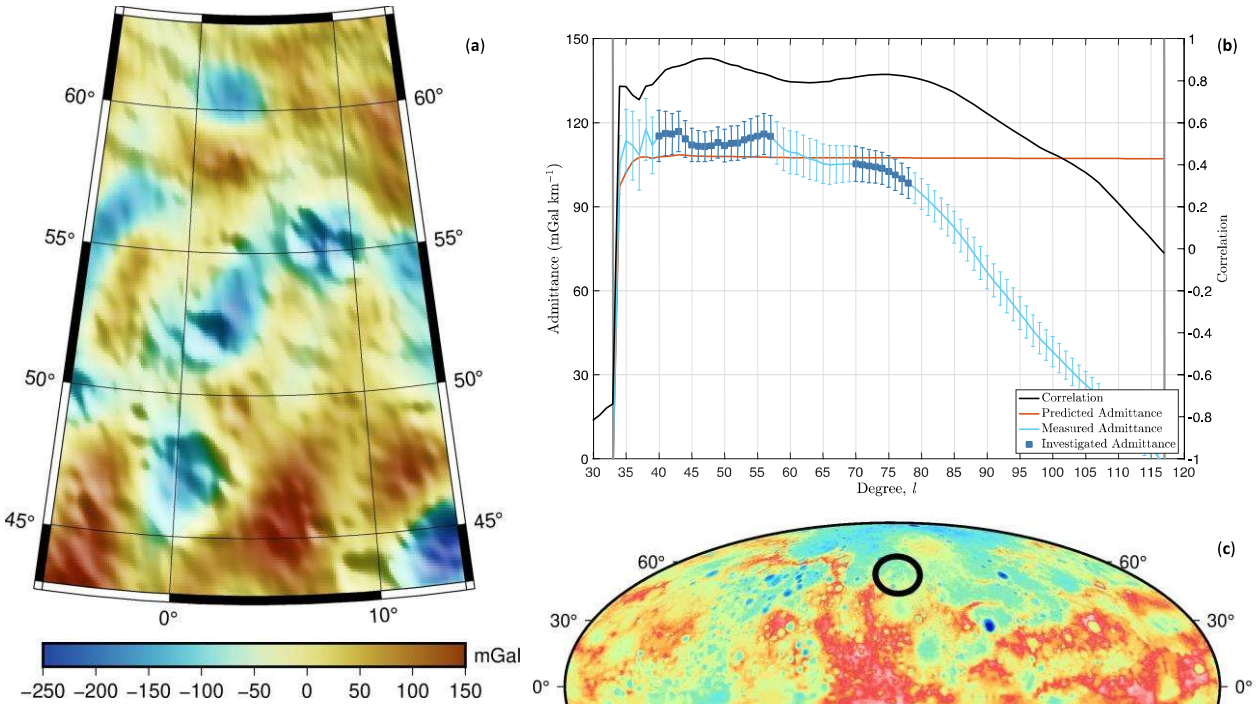

Figure 5 (**a**) Local map of free-air gravity anomaly (mGal) shown over shaded topographic relief in a Lambert Conformal Conic projection, and (**b**) correlation and admittance between gravity and topography localized on (**c**) a spherical cap centered at 4°E longitude and 53°N latitude. The localization windowing is carried out with a 10° radius, a concentration factor of 0.999 ($L_{win} = 33$), and a spherical harmonic expansion to degree $l_{max} = 148$ (see caption of Figure 3 for more details).

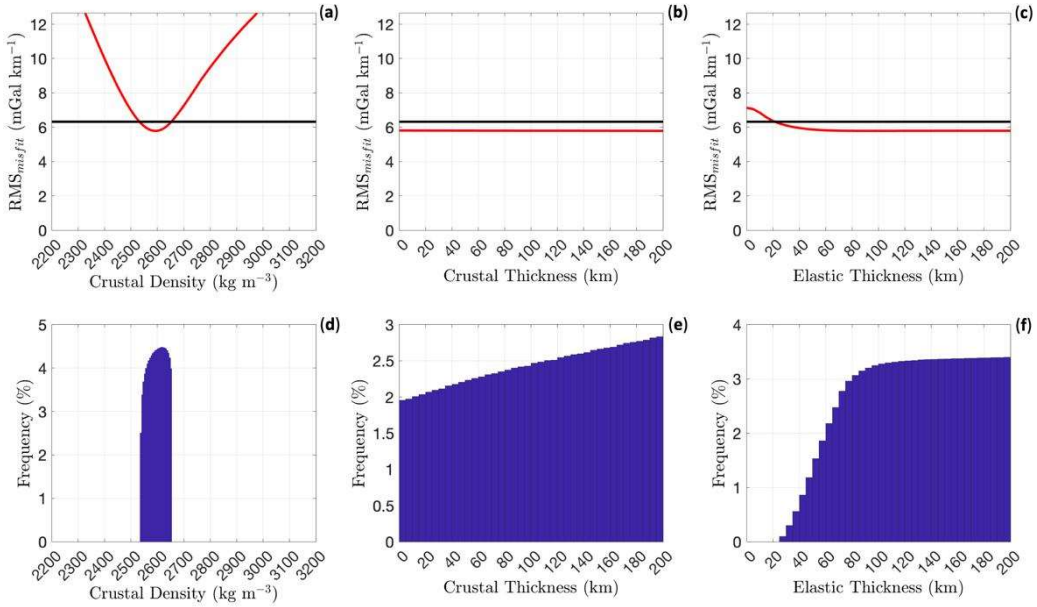

Figure 6 (**a-b-c**) Misfit plots and (**d-e-f**) histograms for the crustal density and thickness, and elastic thickness resulting from the comparison between measured and predicted localized admittance shown in Figure 5-b. The black horizontal line shows the RMS of the formal uncertainties of the local admittance, $\overline{\sigma}$, and the red curve the RMS_{misfit}as function of the estimated parameter.

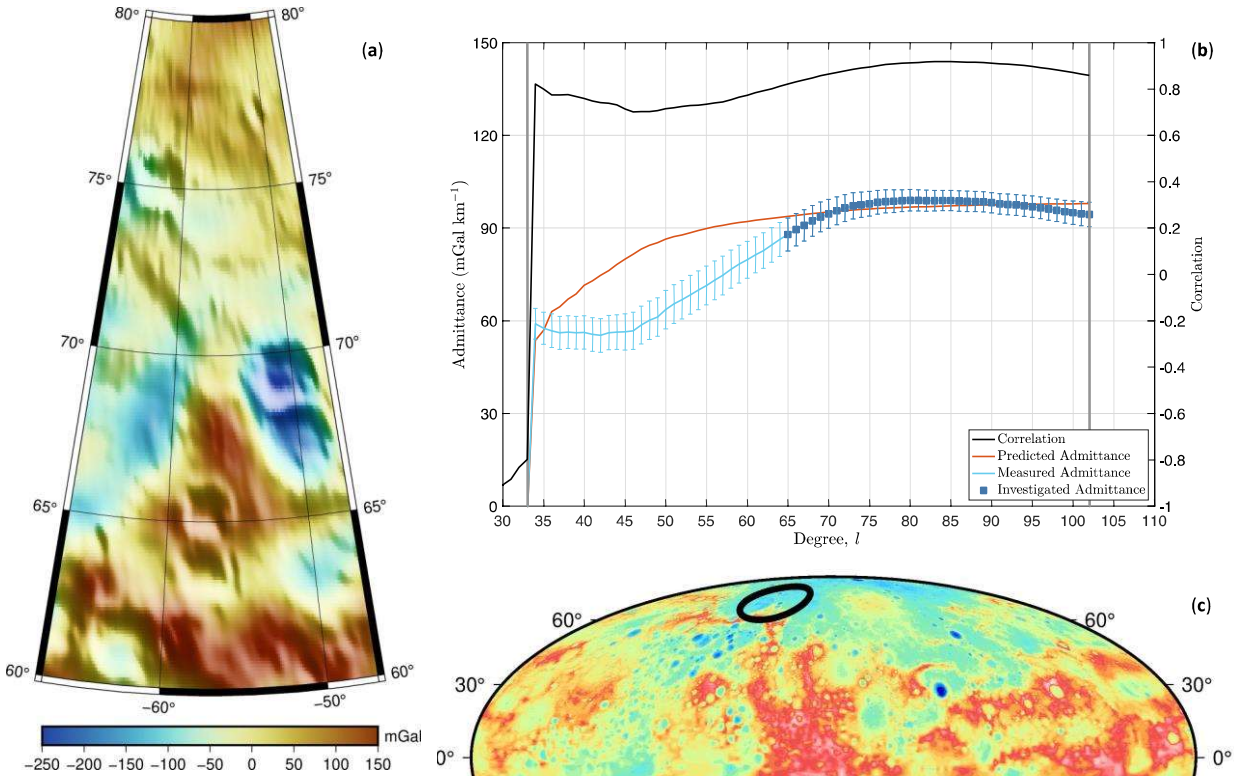

Figure 7 (**a**) Local map of free-air gravity anomaly (mGal) shown over shaded topographic relief in a Lambert Conformal Conic projection, and (**b**) correlation and admittance between gravity and topography localized on (**c**) a spherical cap centered at 303°E longitude and 70°N latitude. The localization windowing is carried out with a 10° radius, a concentration factor of 0.999 ($L_{win} = 33$), and a spherical harmonic expansion to degree $l_{max} = 135$ (see caption of Figure 3 for more details).

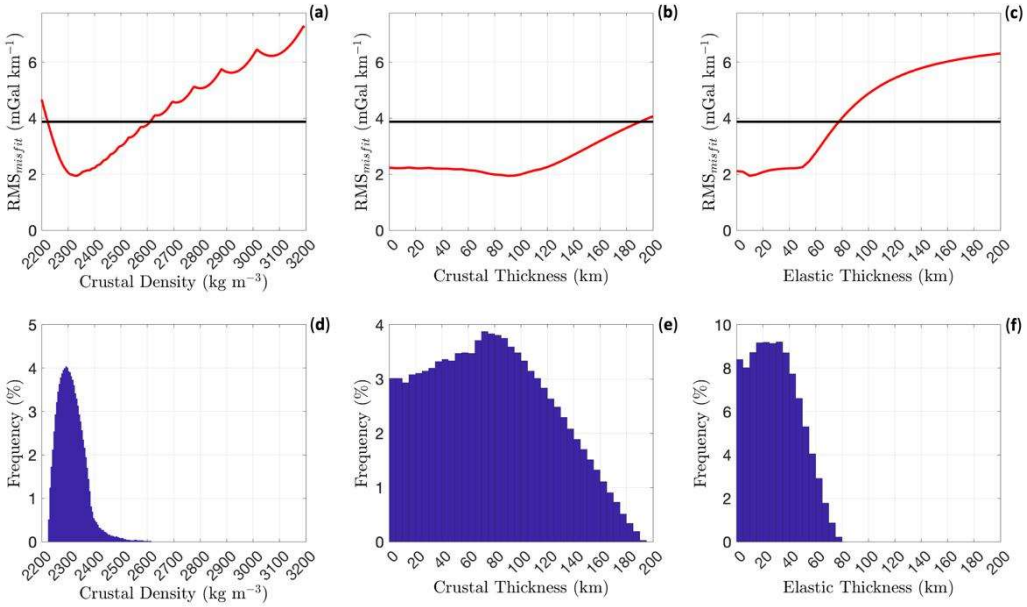

Figure 8 (**a-b-c**) Misfit plots and (**d-e-f**) histograms for the crustal density and thickness, and elastic thickness resulting from the comparison between measured and predicted localized admittance shown in Figure 7-b. The black horizontal line shows the RMS of the formal uncertainties of the local admittance, $\overline{\sigma}$, and the red curve the RMS_{misfit}as function of the estimated parameter.

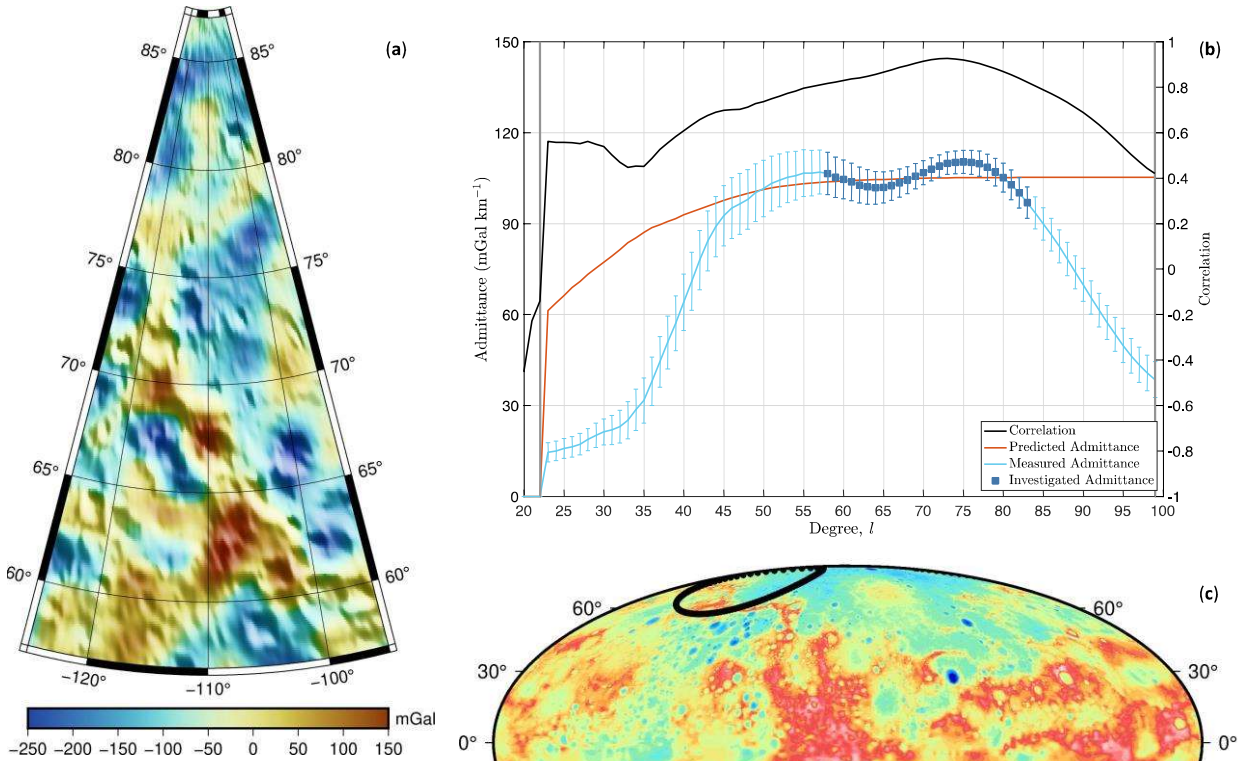

Figure 9 (**a**) Local map of free-air gravity anomaly (mGal) shown over shaded topographic relief in a Lambert Conformal Conic projection, and (**b**) correlation and admittance between gravity and topography localized on (**c**) a spherical cap centered at 250°E longitude and 72°N latitude. The localization windowing is carried out with a 15° radius, a concentration factor of 0.999 ($L_{win} = 22$), and a spherical harmonic expansion to degree $l_{max} = 121$ (see caption of Figure 3 for more details).

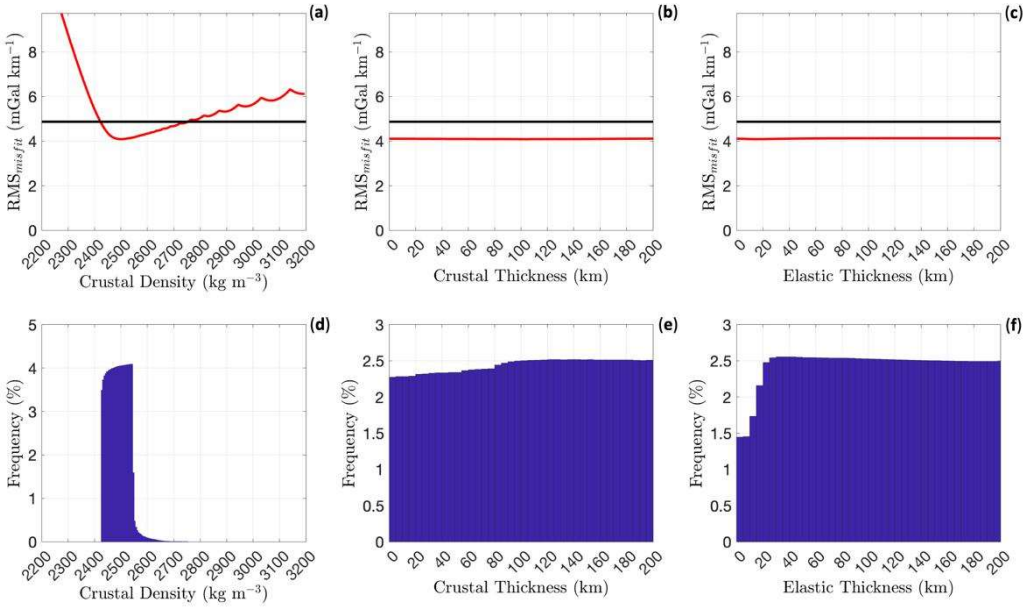

Figure 10 (**a-b-c**) Misfit plots and (**d-e-f**) histograms for the crustal density and thickness, and elastic thickness resulting from the comparison between measured and predicted localized admittance shown in Figure 9-b. The black horizontal line shows the RMS of the formal uncertainties of the local admittance, $\overline{\sigma}$, and the red curve the RMS_{misfit}as function of the estimated parameter.

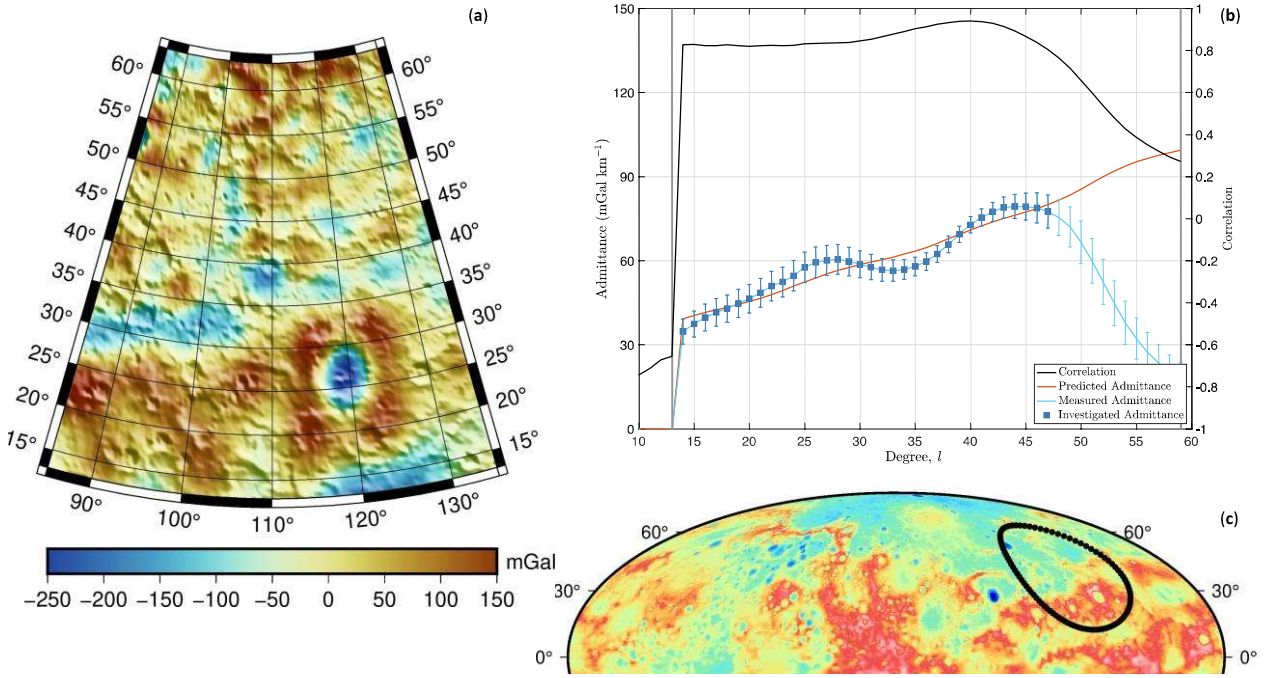

Figure 11 (**a**) Local map of free-air gravity anomaly (mGal) shown over shaded topographic relief in a Lambert Conformal Conic projection, and (**b**) correlation and admittance between gravity and topography localized on (**c**) a spherical cap centered at 110°E longitude and 38°N latitude. The localization windowing is carried out with a 25° radius, a concentration factor of 0.999 ($L_{win} = 13$), and a spherical harmonic expansion to degree $l_{max} = 72$ (see caption of Figure 3 for more details).

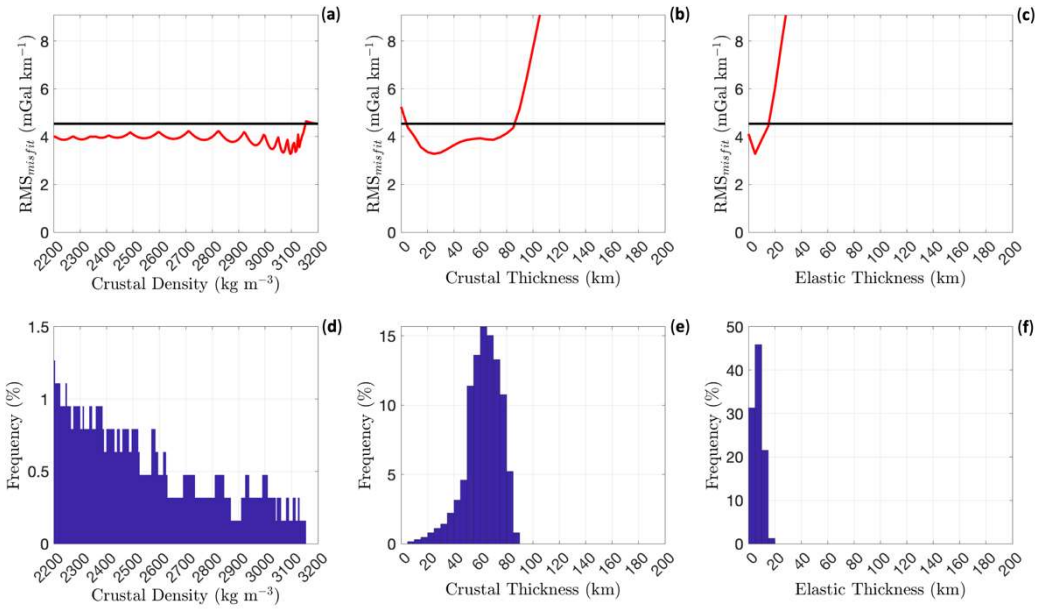

Figure 12 (**a-b-c**) Misfit plots and (**d-e-f**) histograms for the crustal density and thickness, and elastic thickness resulting from the comparison between measured and predicted localized admittance shown in Figure 11-b. The black horizontal line shows the RMS of the formal uncertainties of the local admittance, $\overline{\sigma}$, and the red curve the RMS_{misfit}as function of the estimated parameter.

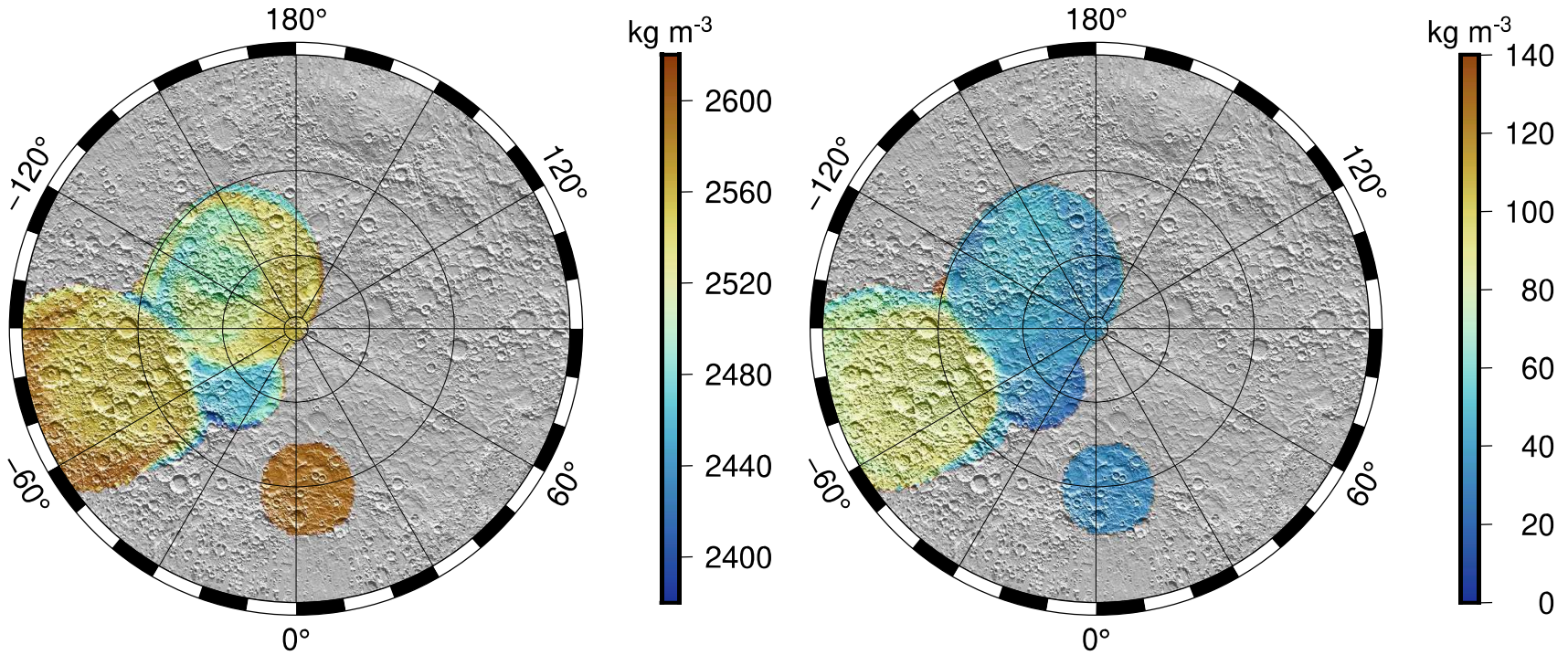

Figure 13 Maps of the lateral variations of the (**left**) crust bulk density and (**right**) its uncertainty in a polar stereographic projection from 30ºN-latitude. Grey colors show regions where the localized gravity/correlation admittance spectra do not allow to constrain the crustal density.

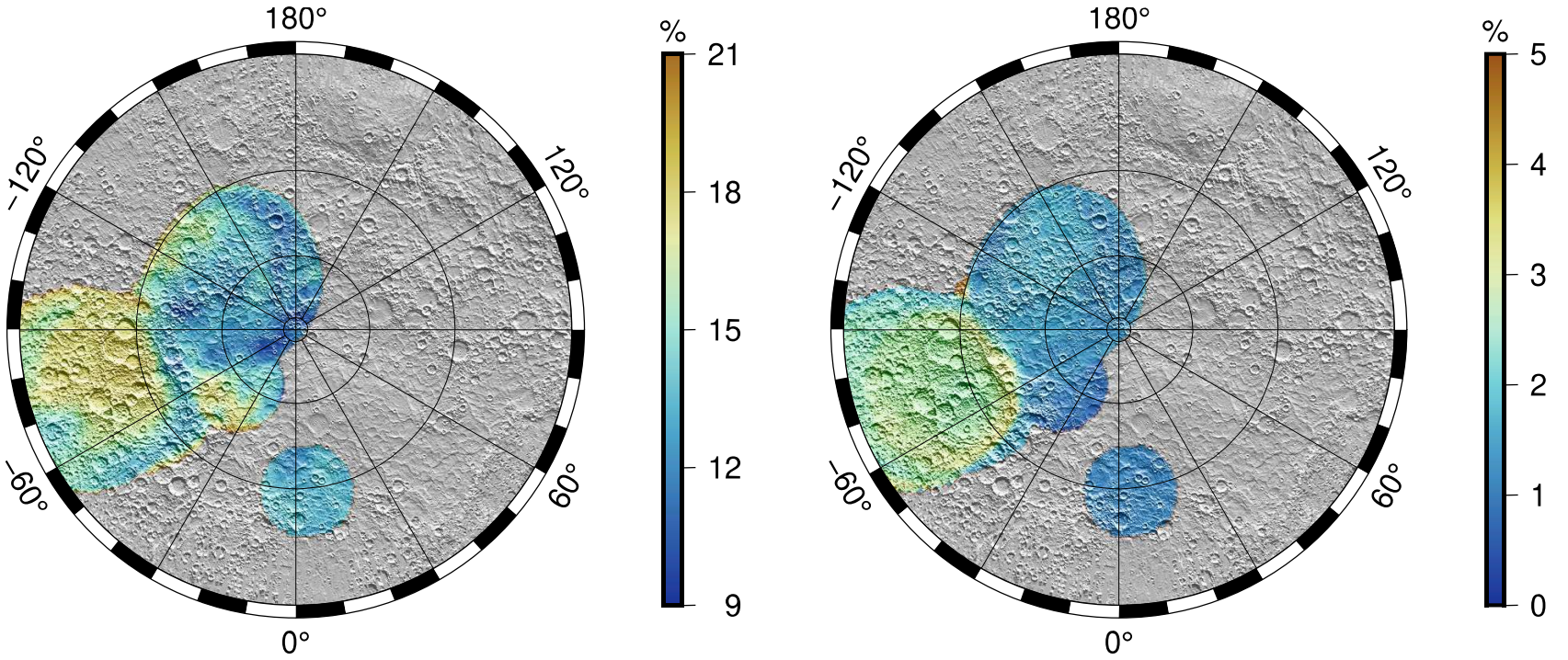

Figure 14 Maps of the lateral variations of the (**left**) surface porosity and (**right**) its uncertainty in a polar stereographic projection from 30ºN-latitude. The lateral variations of the surface porosity are computed by comparing the bulk density retrieved from local admittance analyses and the grain density reported by Beuthe et al. 2020